The near wake of discrete roughness elements on swept wings

Zoppini, G.; Michelis, T.; Ragni, D.; Kotsonis, M.

DOI
10.1017/jfm.2023.141

Publication date
2023

Document Version
Final published version

Published in
Journal of Fluid Mechanics

J. Fluid Mech. (2023), *vol*. 960, A11, doi:10.1017/jfm.2023.141

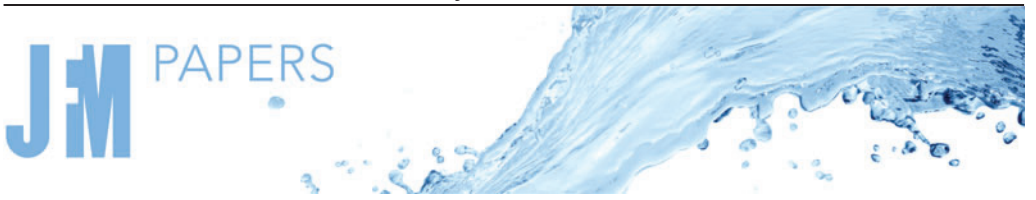

The near wake of discrete roughness elements on swept wings

G. Zoppini[1],†, **T. Michelis**[1], **D. Ragni**[2] **and M. Kotsonis**[1]

[1]Section of Aerodynamics, Delft University of Technology, 2629 HS Delft, The Netherlands

[2]Group of Aeroacoustics, Delft University of Technology, 2629 HS Delft, The Netherlands

(Received 2 August 2022; revised 7 February 2023; accepted 11 February 2023)

This work presents the first experimental characterization of the flow field in the vicinity of periodically spaced discrete roughness elements (DRE) in a swept wing boundary layer. The time-averaged velocity fields are acquired in a volumetric domain by high-resolution dual-pulse tomographic particle tracking velocimetry. Investigation of the stationary flow topology indicates that the near-element flow region is dominated by high- and low-speed streaks. The boundary layer spectral content is inferred by spatial fast Fourier transform (FFT) analysis of the spanwise velocity signal, characterizing the chordwise behaviour of individual disturbance modes. The two signature features of transient growth, namely algebraic growth and exponential decay, are identified in the chordwise evolution of the disturbance energy associated with higher harmonics of the primary stationary mode. A transient decay process is instead identified in the near-wake region just aft of each DRE, similar to the wake relaxation effect previously observed in two-dimensional boundary layer flows. The transient decay regime is found to condition the onset and initial amplitude of modal crossflow instabilities. Within the critical DRE amplitude range (i.e. affecting boundary layer transition without causing flow tripping) the transient disturbances are strongly receptive to the spanwise spacing and diameter of the elements, which drive the modal energy distribution within the spatial spectra. In the super-critical amplitude forcing (i.e. causing flow tripping) the near-element stationary flow topology is dominated by the development of a high-speed and strongly fluctuating region closely aligned with the DRE wake. Therefore, elevated shears and unsteady disturbances affect the near-element flow development. Combined with the harmonic modes transient growth these instabilities initiate a laminar streak structure breakdown and a bypass transition process.

Key words: boundary layer receptivity, boundary layer stability, transition to turbulence

† Email address for correspondence: g.zoppini@tudelft.nl

1. Introduction

Laminar to turbulent transition of swept wing boundary layers (BLs) in low turbulence environments is dominated by the development of stationary crossflow instabilities (CFI, Bippes 1999; Wassermann & Kloker 2002; Saric, Reed & White 2003; Serpieri & Kotsonis 2016). The onset and downstream evolution of stationary CFI is highly sensitive to surface roughness (Radeztsky, Reibert & Saric 1999; Saric *et al.* 2003) including the residual small-amplitude distributed roughness of the wing surface finishing. Therefore, many experimental and numerical works dedicated to the investigation of CFI apply an artificial forcing in the form of arrays of discrete roughness elements (DRE) periodically arranged along the wing span (Reibert *et al.* 1996; Saric, Carrillo & Reibert 1998; Serpieri & Kotsonis 2016). The resulting BL flow is spanwise uniform and is dominated by the development of a monochromatic stationary CFI mode, developing with the same spanwise wavelength as the one corresponding to the DRE inter-spacing.

The process through which external disturbances enter the BL and convert into modal perturbations is called receptivity (Morkovin 1969) and is still posing a significant challenge towards the elucidation of swept wing transition. In fact, despite the widespread use of DRE (or equivalent discrete forcing methods) in experimental and numerical studies, only a few numerical simulations focussed on the characterization of the near-element flow features in three-dimensional (3-D) BLs (Kurz & Kloker 2014, 2016; Brynjell-Rahkola *et al.* 2017). The direct investigation of these flow features could give fundamental insights into the initial phases of the receptivity process. However, the characterization of the near-element flow in an experimental context is limited by two main factors. On the one hand, due to the diverse and disparate scales of the flow phenomena involved, the near-element flow region is posing considerable challenges for state-of-art flow measurement techniques. As an example, the investigation presented in this work is performed on a swept wing model of more than 1 m chord and span, developing a BL characterized by $\delta_{99} \simeq 1.4$ mm at 15 % chord (Serpieri & Kotsonis 2015). On the other hand, despite being mostly affected by surface roughness, numerous other parameters (such as free-stream turbulence, local pressure gradient and possible non-modal interactions in the element vicinity) are also involved in the receptivity process. These aspects complicate the implementation of numerical prediction tools capable of thoroughly simulating the near-element flow features. Lastly, a unifying feature that further increases the challenge in understanding these processes is the high three-dimensionality of the local flow, as shown by Kurz & Kloker (2014, 2016). Accordingly, the investigation of such a flow scenario requires the use of volumetric velocity measurement techniques. Notwithstanding the intricacies of the problem, the direct numerical simulation (DNS) investigations conducted by Kurz & Kloker (2014, 2016) and Brynjell-Rahkola *et al.* (2017), provide a detailed description of the DRE near-element flow topology. These works identified the dominant flow structures and their behaviour in super-critical and critical amplitude forcing configurations. Throughout this work the definition of super-critical amplitude forcing configurations applies to forcing cases with sufficiently high DRE amplitude to induce flow transition in the vicinity of the roughness array, preventing the development of modal instabilities. Critical amplitude forcing configurations instead induce a set of instabilities in the DRE vicinity that develops into stationary modal CFI downstream, which ultimately drive the BL flow transition to turbulence. In both scenarios, a recirculation region is identified immediately aft of the element. This is accompanied by the formation of a complex set of vortical systems that develop around the element. Specifically, a pair of counter-rotating horseshoe vortex (HSV) legs originating from the roll-up of the BL streamwise vorticity upstream of the element, develops from the

element's flanks. In turn, these HSV legs induce a weaker inner pair of counter-rotating vortices through the lift-up effect (Landahl 1980). The development of such vortical systems compares well with the flow field incurred by an isolated discrete roughness element or a DRE array in 2-D BLs (Baker 1979; Klebanoff, Cleveland & Tidstrom 1992; Ergin & White 2006; Kurz & Kloker 2016). Additionally, a dedicated investigation conducted by the authors experimentally measures the near-wake flow of an isolated element in a 3-D BL, observing comparable flow topology and structure development (Zoppini, Ragni & Kotsonis 2022*a*). For the sake of clarity, throughout this work the distinction between the near-wake and far-wake region is based on the chord location at which the primary stationary disturbance recovers a modal behaviour (i.e. $x/c = 0.164$ in the present work), thus growing exponentially further downstream (i.e. in the far wake). This aspect is further discussed in § 3.1 and illustrated in figure 7. However, the downstream evolution of the vortical structures in the far wake of the roughness element shows significant differences between the 2-D and 3-D BLs. Namely Kurz & Kloker (2016) showed that the presence of the crossflow velocity component in the swept wing base flow leads to a loss of flow symmetry, as the resulting flow field is dominated by the crossflow direction of rotation. Accordingly in 3-D BLs vortical structures co-rotating with the CFI (defined as co-crossflow structures for the sake of brevity) are sustained in their downstream evolution, while the counter-rotating structures are damped. As a result, only one leg of each vortical system is sustained in the flow field either initiating the development of modal instabilities or driving the laminar breakdown of the streak structures and the onset of turbulence (i.e. causing bypass transition). The latter case typically occurs in the presence of super-critical forcing configurations featuring high-amplitude DRE. Due to the strong local wall-normal and spanwise shears, near-wake unsteady instabilities (often of Kelvin–Helmholtz type) with excessive initial amplitude and rapid local growth develop and trigger transition in the element vicinity, effectively bypassing the development of modal CFI (Klebanoff *et al.* 1992; Reshotko 2001; Ergin & White 2006).

Several efforts have been made towards scaling this particular problem. The discrete roughness-induced transition behaviour can be satisfactorily predicted based on the roughness Reynolds number i.e. $Re_k = (k \times |\boldsymbol{u}(k)|)/\nu$ (Gregory & Walker 1956; Tani 1969; Klebanoff *et al.* 1992). This geometrical parameter accounts for the element height (k) and local BL development through $|\boldsymbol{u}(k)|$ (i.e. the local undisturbed BL velocity at k) and ν (the kinematic viscosity). Specifically for low Re_k (i.e. $Re_k < 200$ for the current experimental set-up, also used in Zoppini *et al.* 2022*b*) the sustained HSV leg is amplified past the element far wake and develops into a modal stationary crossflow vortex. For higher Re_k the recirculation region forming aft of the element is strong enough to amplify unsteady disturbances in the wake-induced shear layer, which provide the first seed for unsteady laminar breakdown (Acarlar & Smith 1987; Klebanoff *et al.* 1992; Zoppini *et al.* 2022*a*). As such these near-wake instabilities persist and grow in the wake flow field, contaminating the laminar flow regions and initiating the BL transition to turbulence shortly downstream of the element location (Kurz & Kloker 2016; Brynjell-Rahkola *et al.* 2017). Previous investigations showed that comparable behaviour characterizes 2-D BLs forced by isolated roughness elements or DRE arrays (e.g. Klebanoff *et al.* 1992; Ergin & White 2006; Casacuberta *et al.* 2019; Bucci *et al.* 2021).

Despite the significant insights on the near-element flow topology and instability development offered by the discussed DNS studies, the characterization of the DRE–CFI onset relation is yet to be defined. This is particularly evident in the lack of dedicated

experimental studies of these effects. Nonetheless, a wider body of literature is dedicated to the investigation of the near-wake features induced by roughness elements in 2-D BLs (e.g. White, Rice & Ergin 2005; Tempelmann, Hanifi & Henningson 2012*a*; Cherubini *et al.* 2013; Bucci *et al.* 2021). In particular, many of the reported works identify transient growth as a fundamental mechanism occurring in the near-wake region, relating the downstream onset of modal instabilities (i.e. critical behaviour) or the occurrence of bypass transition (i.e. super-critical behaviour) to the initial algebraic growth of the near-wake disturbances. Given the similarities of the near-element flow fields between 2-D and 3-D BL cases, it can be expected that transient growth mechanisms might be active also in the latter. Some evidence of such behaviour was shown by a previous experimental investigation conducted by the authors (Zoppini *et al.* 2022*b*). Furthermore the highly three-dimensional flow developing in the near wake of critical and super-critical roughness elements has been widely investigated through global stability analysis (e.g. Denissen & White 2013; Loiseau *et al.* 2014; Kurz & Kloker 2016). However, in their numerical investigation, Kurz & Kloker (2016) outlined that the instability mechanism dominating the bypass transition scenario is not necessarily a global instability. Rather, depending on Re_k, it can develop as a purely convective instability in the element near wake, further accommodating the possible presence of transient mechanisms in the near-wake flow.

More specifically, transient growth is a linear instability mechanism driving the algebraic amplification of initially small-amplitude disturbances which exponentially decay shortly downstream (e.g. Corbett & Bottaro 2001; Schmid & Henningson 2001; Levin & Henningson 2003; Lucas 2014). This phenomenon typically occurs in shear layers that are otherwise stable to modal instabilities. Transient growth mechanisms govern the linear superposition of individually stable non-orthogonal disturbance modes (e.g. Schmid & Henningson 2001; Lucas 2014). Therefore, the occurrence of such mechanisms in the element's near wake (and consequently in the initial phases of the receptivity process) would relate to the presence of non-modal flow interactions. From a mathematical standpoint, the occurrence of transient growth can be related to the non-normal nature of the Orr–Sommerfeld/Squire operator, which features mutually non-orthogonal eigenmodes (Schmid & Henningson 2001). As such, a disturbance resulting from the linear superposition (i.e. vectorial sum) of individually decaying non-orthogonal solutions of the stability problem (Mack 1984; Herbert 1993) can experience algebraic growth.

From a physical point of view the transient growth process can be related to the presence of a lift-up mechanism (Landahl 1980) characterizing flow fields dominated by instabilities in the form of streamwise structures (Corbett & Bottaro 2001; Reshotko 2001; Henningson 2006). Specifically in the case of DRE embedded in a laminar 3-D BL a disturbance in the form of a streamwise vortex will transfer momentum across the BL, inducing a strong streamwise velocity perturbation (i.e. streak). The original vortical structures may be locally stable and undergo exponential decay, however, the increased disturbance energy associated with the streamwise momentum redistribution can exceed the energy decay of the streak, thus leading to transient growth (Landahl 1980; Breuer & Kuraishi 1994; Corbett & Bottaro 2001). The transient growth phase is typically brief, albeit intense, and is rapidly hindered by the exponential decay of the energy associated with the dominant modes (Schmid & Henningson 2001; Henningson 2006). Nonetheless, its occurrence drives the growth of the near-wake instabilities, conditioning the onset of modal instabilities (Breuer & Kuraishi 1994; Corbett & Bottaro 2001; Lucas 2014; Zoppini *et al.* 2022*b*) or inducing rapid laminar breakdown (i.e. bypass transition) depending on the achieved amplitude peak (Andersson, Berggren & Henningson 1999; Reshotko 2001). Specifically, in a 3-D BL forced by DRE amplitudes corresponding to low Re_k,

the evolution of the transient near-wake instabilities can determine the initial amplitude of the triggered modal instabilities with important consequences for their downstream growth and eventual transition (Breuer & Kuraishi 1994; Corbett & Bottaro 2001; Lucas 2014).

The experimental investigations by White & Ergin (2003) and White *et al.* (2005) showed that, in 2-D BLs, algebraic growth is a fundamental mechanism in the near-wake flow evolution. The analysis of the spatial Fourier energy distribution indicates that the observed transient process is mainly sustained by the third and fourth harmonics of the dominant stationary mode (corresponding to the wavelength forced by the applied DRE array). The modal energy associated with such harmonics grows algebraically immediately aft of the element, followed by exponential decay shortly after while scaling with Re_k^2 in the transient flow region. These results have been confirmed by the DNS investigation by Fischer & Choudhari (2004), albeit overestimating the modal energy measured in the experiments. Furthermore, previous investigations dedicated to 2-D BL receptivity characterized the near wake of DRE of various shapes (i.e. square, hump, micro-ramp and cylinders) and sizes (represented by the height-to-diameter ratio of the considered geometries) (e.g. Rizzetta *et al.* 2010; Ye, Schrijer & Scarano 2016). Both these parameters appear to affect the near-wake velocity field to such an extent that differences could be observed in the spanwise frequency spectra incurred by the different geometries. Accordingly, already the modification of the roughness height-to-diameter (k/d) ratio can affect the identified transient growth phenomena and consequently the onset of modal CFI, as outlined by White *et al.* (2005). However, White *et al.* (2005) describe relatively simple modelling functions based on the element geometry and on the chordwise location of the modal energy peak that approximate well the observed transient energy growth of the harmonic modes.

Previous investigations conducted by the authors dedicated to the DRE near wake in a 3-D BL (Zoppini *et al.* 2022*b*) also identified the occurrence of a transient mechanism with modal energy distribution comparable to White *et al.* (2005). However, in the cited investigation the spatial resolution of the experimental measurements was insufficient to identify the algebraic growth of the instabilities, which is a fundamental trait of the transient growth process. Accordingly, the role of the transient growth mechanism in conditioning the onset of modal instabilities as well as their dependence on the external forcing configuration could not be clearly outlined. The available literature framework shows that the receptivity process of forcing cases with sub-critical forcing amplitude (i.e. originating weak CFI that only marginally affect the transitional process) can be approximated by a direct geometrical dependence of the initial modal amplitude on the DRE geometry. This applies to forcing configurations in which the initial CFI amplitudes scale with the element geometry either represented by the simple element height (k, Schrader, Brandt & Henningson 2009; Tempelmann *et al.* 2012*b*) or by a geometrical parameter such as Re_k (expressing a dependence on k^2). The former cases feature very low forcing amplitude configurations (i.e. k lower than 10 % of the local BL displacement thickness, Hunt & Saric 2011; Tempelmann *et al.* 2012*b*). The latter instead includes the results by Kurz & Kloker (2014) outlining that the receptivity process of roughness elements with height lower than 30 % of the local BL displacement thickness is described by a receptivity coefficient that linearly depends on k (hence the initial amplitude of the modal CFI relates to k^2). This behaviour is particularly evident for configurations with varying DRE aspect ratio (k/d, e.g. increasing height for a constant DRE diameter), while the initial amplitude sensitivity to the element height is reduced for constant aspect ratio geometries (Kurz & Kloker 2014). Evidently, the complexity of receptivity under variations of a multitude of governing parameters (such as roughness height, diameter,

location etc.) complicates the deterministic definition of specific receptivity regimes. Nonetheless, to classify these receptivity regimes in intuitively accessible terms, throughout this work the aforementioned configurations are grouped under the k-dependent receptivity definition as they are represented through a direct relation with k showing only minor dependence on the effective DRE shape. It must be stressed here that k-dependent receptivity does not exclude dependence on other parameters (such as diameter or geometrical shape), but rather denotes the dominant influence of roughness height on the conditioning of the initial modal amplitudes. Higher amplitude elements follow a receptivity process with no clearly outlined dependence on the external forcing geometry. Therefore, a clear receptivity model for the characterization of the critical amplitude cases considered in the present work is still missing. Additionally, in the super-critical amplitude forcing the near-wake flow receptivity is likely dominated by mechanisms leading to bypass transition processes (Andersson *et al.* 1999; Ergin & White 2006; Kurz & Kloker 2016).

The above-surveyed works highlight the importance of near-wake mechanics in the analysis of receptivity to roughness elements. Nevertheless, a systematic experimental flow field exploration in 3-D BLs (i.e. swept wings) is currently not available. As such, the current work aims at deepening the near-wake flow analysis, confirming the presence of transient growth mechanisms and characterizing their role in the initial conditioning of the modal CFI. In particular, the BL receptivity to DRE arrays of various amplitudes is characterized, delivering a conceptual model detailing the 3-D BL receptivity to critical and super-critical DRE, thus extending the transitional paths model proposed by Morkovin, Reshotko & Herbert (1994). A first-of-its-kind experimental investigation of the near-element flow field is provided, accessing the 3-D time-averaged velocity fields in the element vicinity through specialized high-resolution dual-pulse tomographic particle tracking velocimetry (PTV) and the shake-the-box algorithm. The presented experimental data detail the near-element stationary flow topology and identify the dominant flow structures and their spatial organization both for critical and super-critical DRE amplitudes. The modal composition of the flow field is investigated by means of a spanwise spatial spectral analysis. Additionally, the high spatial resolution of the acquired data details the total perturbation as well as the amplitude and energy growth associated with individual modes in the element near-wake region. Finally, the flow development is monitored under varying DRE configurations, investigating the receptivity of instabilities to the forcing amplitude and wavelength.

2. Methodology

2.1. *Swept wing model, wind tunnel and flow stability*

The experimental measurements presented in this work are performed using an in-house designed swept wing model extensively described in Serpieri & Kotsonis (2015). The wing features a constant streamwise chord ($c = 1273$ mm) and a sweep angle of 45°. A favourable pressure gradient characterizes the wing up to $x/c = 0.63$ thus allowing thorough investigation of primary and secondary CFI and ensuing BL transition (Serpieri & Kotsonis 2016). Additionally, given the high sensitivity of CFI to surface roughness, the wing surface is carefully polished, ensuring a low and uniform roughness level ($R_q = 0.2$ μm, Serpieri & Kotsonis 2015).

The presented measurements are performed in the low-speed Low Turbulence wind Tunnel (LTT) at TU Delft, an atmospheric closed return tunnel featuring low free-stream turbulence level in the test section flow. Specifically, at the tested conditions the

free-stream turbulence level is $T_u = 0.025\,\%$ of the free-stream speed in the 2–5000 Hz frequency band (Serpieri 2018). All measurements are performed at a fixed angle of attack ($\alpha = -3.36^\circ$) and various free-stream Reynolds numbers ($Re_c = 1.35 \times 10^6$, 1.85×10^6, 2.17×10^6). Stability solutions are computed for the three measured Re_c based on a steady and incompressible solution of the 2.5-D BL equations and linear stability theory (LST, Mack 1984). The procedure followed is extensively described in Serpieri (2018) and is omitted here for the sake of brevity. Referring to the $Re_c = 2.17 \times 10^6$ case, the computed stability solutions predict the wavelength and evolution of the most unstable mode ($\lambda_1 = 8$ mm), providing a reliable basis for the experimental forcing configurations design.

The xyz reference system used in this work has its x and z axes orthogonal and aligned to the leading edge, respectively, with corresponding velocity components u, v, w. Throughout this work, the wall-normal direction (y) is non-dimensionalized by the experimentally measured unperturbed (i.e. no DRE applied) BL displacement thickness at $x/c = 0.165$ for $Re_c = 2.17 \times 10^6$, hereafter defined $\delta^* = 0.46$ mm.

2.2. *Spanwise periodic DRE*

As previously discussed, numerous investigations dedicated to CFI apply DRE arrays on the wing surface towards focussing the BL development into a single monochromatic mode (e.g. Reibert *et al.* 1996; Saric *et al.* 2003). In the current application, the forced mode (i.e. the inter-spacing of the elements λ_{f1}) is chosen to coincide with the wavelength of the most unstable stationary CFI mode λ_1, corresponding to 8 mm, as predicted by LST and found in previous works (Serpieri 2018). Typically, the DRE array is applied in the vicinity of the forced mode neutral point, thus close to the wing leading edge. However, recent investigations by the authors (Zoppini *et al.* 2022*b*) showed that this forcing configuration can be geometrically upscaled and moved at further downstream and experimentally more accessible chord locations. In particular, in the present measurements the DRE arrays are placed at $x_{DRE}/c = 0.15$, where the unperturbed (i.e. no DRE applied) experimental BL displacement thickness is $\delta^* = 0.44$ mm (corresponding to $\delta_{99} = 1.4$ mm). In comparison, the boundary layer thickness at $x/c = 0.02$ is estimated to be $\delta^* = 0.14$ mm (corresponding to $\delta_{99} = 0.6$ mm). While still extremely thin, the BL at $x/c = 0.15$ is sufficiently thick to be measured by the high spatial resolution optical velocimetry technique used in this work. Additionally, the local growth rate of the modal CFI can be described by $\partial N/\partial x$, where N is the N-factor evolution provided by the LST solution at $Re_c = 2.17 \times 10^6$. The $\partial N/\partial x$ value at $x/c = 0.15$ is comparable to the value obtained in the vicinity of the dominant mode neutral point (i.e. within a 10 % difference), further validating the possibility of investigating the near-wake flow development for the downstream applied DRE array.

Various forcing configurations are investigated to characterize the receptivity of the near-element flow features to the DRE amplitude (k) and forcing wavelength (λ_{f1}). Specifically, four different element heights (nominally $k_1 = 0.1$ mm, $k_2 = 0.2$ mm, $k_3 = 0.3$ mm and $k_4 = 0.4$ mm) and three different forcing wavelengths are considered. Following the definition of $\lambda_i = \lambda_1/i$, forcing wavelengths $\lambda_{3/2} \simeq 5$ mm, $\lambda_1 \simeq 8$ mm and $\lambda_{2/3} \simeq 11$ mm are measured. Throughout this work, the $\lambda_1 = 8$ mm mode is associated with the most unstable mode at all considered Reynolds number cases. More specifically, stability solutions computed at the lower and higher Re_c indicate that the most unstable CFI mode corresponds to wavelengths of 10 mm to 8 mm, respectively (Zoppini *et al.* 2022*b*). Hence, within the range of Re_c investigated in this work, the

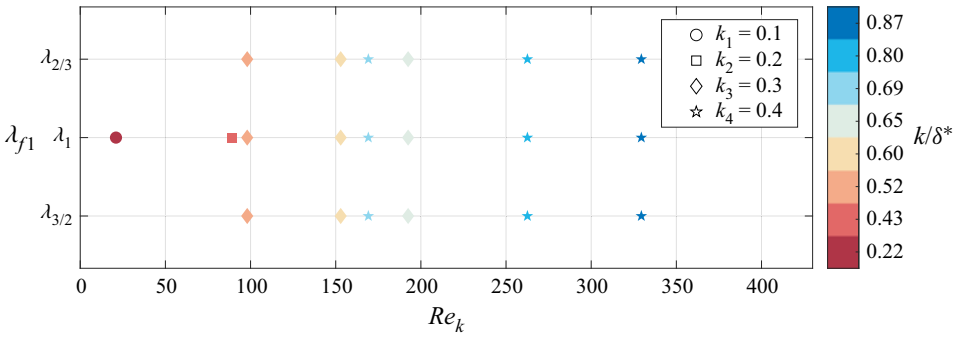

Figure 1. Geometrical parameters of the measured forcing configurations computed from numerical BL solutions. Colour map based on k/δ^*, symbols based on DRE height, legend indicating nominal element height [mm].

$\lambda_1 = 8$ mm mode is either the most unstable mode or among the most unstable modes in the vicinity of x_{DRE}/c.

The DRE elements are manufactured in house by computer numeric controlled (CNC) laser cutting of a 100 μm thickness self-adhesive black polyvinyl chloride (PVC) foil. Various heights can be obtained by pasting multiple layers of foil on top of each other prior to the cutting procedure. Each element is designed to be cylindrical with a diameter of $d =$ 2 mm, however, practical limits in the manufacturing process entail slight deviations in their actual shape. The elements have been fully characterized through a statistical study by using a scanCONTROL 30xx laser profilometer (405 nm wavelength and 1.5 μm reference resolution) to extract their wavelength, diameter and height (table 2, Zoppini *et al.* 2022*b*).

The measured forcing configurations can be described through a purely geometrical scaling by defining the ratio between the DRE height (k) and the unperturbed BL displacement thickness at x_{DRE}/c (k/δ^*, Schrader *et al.* 2009). This parameter can be accompanied by the roughness Reynolds number $Re_k = (k \times |\boldsymbol{u}(k)|)/\nu$ (Gregory & Walker 1956; Reibert *et al.* 1996) also accounting for the local BL evolution. Numerous investigations showed that the receptivity to roughness only depends on k for small DRE amplitudes with a fixed diameter (Tempelmann *et al.* 2012*b*; Kurz & Kloker 2014). However, previous investigations by White *et al.* (2005) showed that, for a 2-D BL, Re_k^2 offers a partial but valuable scaling of the near-element flow evolution. Additionally, Re_k proves successful in predicting the criticality of the considered forcing configurations. In particular, in the present work configurations featuring $Re_k \geqslant 200$ behave super-critically (Zoppini *et al.* 2022*b*), therefore they are only considered in § 4 dedicated to the characterization of the near-element features of super-critical amplitude DRE. The geometrical parameters corresponding to the investigated forcing cases are reported in figure 1. A correlation of the considered cases to previous investigations can be obtained using the Von Doenhoff & Braslow (1961) diagram, relating the critical roughness Reynolds number to the inverse aspect ratio of the forcing elements (i.e. d/k) in 2-D base flows. For the sake of conciseness, a direct graphical comparison is omitted, however, the reference critical and super-critical cases (i.e. $Re_c = 2.17 \times 10^6$ with DRE amplitude k_3 or k_4) respectively correspond to $d/k = 6.7, 5$ and $\sqrt{Re_k} = 13.8, 18.1$. Hence, the critical case falls on the lower bound of the transitional region identified by Von Doenhoff & Braslow (1961), while the super-critical case falls well inside it.

2.3. *Dual-pulse tomographic PTV*

The 3-D velocity distribution in the DRE vicinity is acquired through specialized high-resolution dual-pulse tomographic PTV (Malik & Dracos 1993; Wieneke 2012; Schanz, Gesemann & Schröder 2016). The measured 3-D domain is centred at $x/c = 0.165$ and extends for almost $x/c = 0.027$, $y/\bar{\delta}^* \simeq 6$ and $z/\lambda_1 = 3.5$ in the streamwise, wall-normal and spanwise directions, respectively.

The 3-D measurement volume is illuminated with a Quantel Evergreen Nd:YAG dual cavity laser (200 mJ pulse energy at $\lambda = 532$ nm), optically accessing the test section through a Plexiglas window on the test section floor. Through a suitable optical arrangement, the laser beam is shaped into a 40 mm wide and almost 4 mm thick sheet parallel to the wing surface in the area of interest. The flow is imaged through 4 sCMOS LaVision Imager cameras (2560 × 2160 pixel, 16-bit, 6.5 μm pixel pitch), installed on the outer side of the test section with a tomographic aperture of approximately 45°. Each camera is equipped with a 200 mm lens, a 2X teleconverter and a lens-tilt mechanism adjusted to comply with the Scheimpflug condition. The resulting focal length is 400 mm for each camera, featuring an aperture number $f_\# = 11$ to keep the particles in focus throughout the entire volume depth. The distance between the imaged plane (i.e. the model surface) and the camera sensors is ≃1 m, resulting in a magnification factor of ≃0.41 and spatial resolution of 67 px mm^{-1}. The flow is seeded by dispersing 0.5 μm droplets of a water–glycol mixture in the wind tunnel circuit.

For each investigated configuration, 4000 image pairs are acquired at a frequency of 15 Hz. The time interval between paired images is set to 8 μs, corresponding to a free-stream particle displacement of almost 10 px. A dual layer target is used for calibrating the tomographic imaging system, further correcting the obtained mapping functions using the volume self-calibration procedure (Wieneke 2008; Schanz *et al.* 2012). The resulting calibration uncertainty is ≃0.04 px. The image pairs are processed in LaVision DaVis 10 through a shake-the-box, 2-pulse algorithm (Wieneke 2012; Schanz *et al.* 2016) estimating the 3-D velocity field within the acquired volume. The LaVision DaVis 10 processing also provides an estimate of the velocity uncertainties (Janke & Michaelis 2021), which for the present case average to 1.8 % of the local velocity in the BL region. An in-house developed Matlab routine is then employed to perform trajectory binning and conversion to a Cartesian grid. The final vector spacing results in approximately 0.25 mm in the xz plane and 0.04 mm along the y-direction.

2.4. *Velocity field reconstruction and processing*

The time-averaged ($\bar{u}$, $\bar{v}$, $\bar{w}$) and standard deviation (u', v', w') velocity fields are obtained for all three velocity components in the xyz domain. For the sake of conciseness, the main data processing techniques adopted throughout this work are hereafter briefly described as applied to $\bar{u}$, while the treatment of $\bar{v}$ and $\bar{w}$ follows a similar procedure. The wall-normal BL velocity profile ($\bar{u}_b$) is estimated by averaging the $\bar{u}$ velocity signal along z for each fixed xy location. At each chordwise location, the free-stream velocity $\bar{u}_\infty$ is estimated as the average of $\bar{u}_b$ for $y > \delta_{99}$ and its value at $x/c = 0.165$ is used to non-dimensionalize the three velocity components. The disturbance velocity field ($\bar{u}_d$) is computed at each (x, y_*, z) as $\bar{u}_d = \bar{u}(x, y_*, z) - \bar{u}_b(x, y_*)$, with y_* representing a fixed wall-normal location. The analysis of such velocity fields allows for the extraction of the amplitudes of the high- and low-speed streaks (Andersson *et al.* 2001). The wall-normal disturbance velocity profile ($\langle\bar{u}\rangle_z$) is computed as the root mean square of the $\bar{u}_d$ velocity signal along z (Reibert *et al.* 1996; Tempelmann *et al.* 2012*b*). Furthermore, a spatial fast Fourier transform

(FFT) analysis is performed on the spanwise velocity signal at each xy location ($\mathrm{FFT}_z(\bar{u})$), characterizing the BL spectral composition as well as the development of the dominant spanwise mode and its harmonics. This allows for the computation of the total and the modal (i.e. per individual FFT mode) instability amplitude by integrating respectively $\langle\bar{u}\rangle_z$ or the individual FFT mode shape functions along y up to the local BL δ_{99} (Reibert *et al.* 1996; Downs & White 2013). This provides an estimation of the velocity disturbances' growth and evolution along the airfoil chord. Following White *et al.* (2005), the CFI energy is instead computed as $E(\bar{u}) = \int_0^{\delta_{99}} (\langle\bar{u}\rangle_z)^2 \,\mathrm{d}y$. The summation of the disturbance energy associated with each of the three velocity components provides the total disturbance energy $E(\bar{\boldsymbol{u}})$. Similar processing is applied to the individual FFT shape functions to compute the modal energy evolution.

By considering all three velocity components available through the tomographic PTV measurement, the 3-D coherent structures dominating the near-wake flow are identified by applying a vortex identification criterion, namely the Q-criterion (Hunt, Wray & Moin 1988). The flow field is first decomposed into its spectral components and is reconstructed accounting for a truncated set of Fourier modes to improve the data signal-to-noise ratio. The reconstructed domain includes the statistically represented flow field incurred by one DRE element and is rotated to obtain a reference frame (x_R, y_R, z_R) with x_R aligned with the crossflow vortex axis, y_R coincident with y, and z_R normal to the $x_R y_R$ plane. The corresponding time-averaged velocity components are named $\bar{u}_R$, $\bar{v}_R$, $\bar{w}_R$.

3. Critical near-element flow

3.1. *Stationary disturbance topology*

Direct characterization of the near-element flow topology and dominant stationary disturbances is obtained through the time-averaged and standard deviation velocity fields. The critical wavelength forcing configuration (i.e. $\lambda_{f1} = \lambda_1$) at $Re_k = 192$ is considered hereafter as the baseline case for the stationary flow topology investigation. The corresponding disturbance velocity field ($\bar{u}_d$) is reported in figure 2(*a–c*), while figure 2(*d–f*) presents the temporal standard deviation contours (u').

Owing to the volumetric measurement, the stationary flow features dominating the near-element flow evolution can be identified in both the xz and yz planes. Specifically, the velocity contours in figure 2(*a–c*) reveal a low-speed streak developing aft of each DRE in correspondence to the element's wake. This low-speed region is accompanied by two high-speed streaks developing on its flanks. The resulting streak alternation corresponds well to the horseshoe vortex legs wrapping around and extending aft of the element, identified by previous investigations (Baker 1979; Kurz & Kloker 2016). In between neighbouring roughness elements the incoming BL maintains a laminar behaviour as the velocity disturbances introduced by each DRE are highly localized in correspondence to the individual element's wake. The identified stationary flow topology closely resembles the near-element flow of isolated DRE in 2-D or 3-D BLs (e.g. Baker 1979; Loiseau *et al.* 2014; Bucci *et al.* 2021; Zoppini *et al.* 2022*a*). This is also in agreement with the findings of Von Doenhoff & Braslow (1961), in which the near-element behaviour of the individual elements of a DRE array was found to be comparable to that of an isolated DRE if they are arranged at a wavelength $\lambda_{f1} > 3d$. Nonetheless, due to the presence of the crossflow velocity component in the base flow, the stationary structures identified in the near-element flow region follow an asymmetric downstream development (Kurz & Kloker 2016; Brynjell-Rahkola *et al.* 2017; Zoppini *et al.* 2022*a*). In particular, in figure 2(*a*) the outboard high-speed streak (denoted by a solid line) is decaying in the

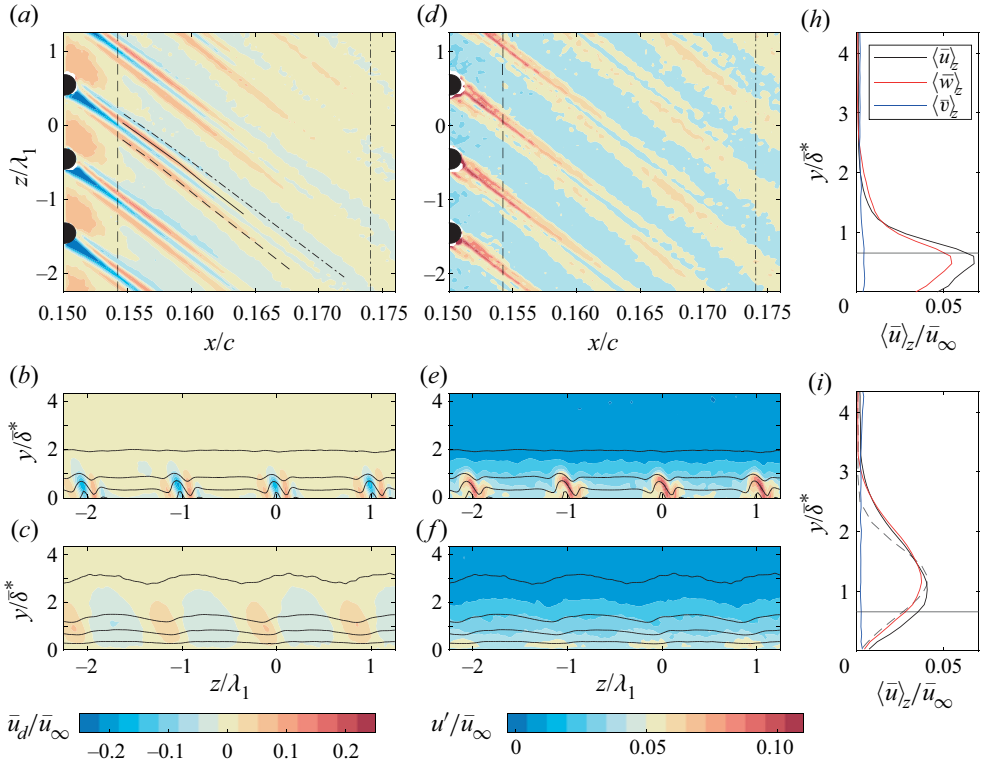

Figure 2. (*a–c*) Values of $\bar{u}_d$ and (*d–f*) u' for forcing case $\lambda_{f1} = \lambda_1$, $Re_k = 192$ (for k_3) in (*a*,*d*) the xz plane at $y = 0.55\bar{\delta}^*$; (*b*,*e*) the yz plane at $x_1 = 0.154c$ (vertical dashed line in *a*,*d*) and (*c*,*f*) at $x_2 = 0.174c$ (vertical dash-dot line in *a*,*d*). Disturbance profiles at (*h*) x_1 and (*i*) x_2 for all three velocity components; element height (solid horizontal black line); LST λ_1 shape function (dashed grey line) scaled to match $\langle\bar{u}\rangle_z$ maximum; element height (horizontal full line).

downstream direction and is substituted by the development of an outboard low-speed streak (denoted by a dash-dot line). Instead, the inboard high-speed streak (indicated by a dashed line) persists until the end of the acquired domain albeit decreasing in amplitude. This results in a far-wake flow dominated by an almost periodic alternation of high- and low-speed regions, respectively induced by the evolution of the inboard high-speed streak and the merging of the outboard low-speed streak and the low-speed wake. The ensuing BL velocity modulation is a typical feature of a modal stationary CFI, resulting from the momentum redistribution across the BL induced by the crossflow vortices (figure 2(*c*), Bippes 1999; Saric *et al.* 2003). Based on the observed development, a near-wake flow region can be defined (i.e. $x/c < 0.164$), which is mostly affected by the stationary streak structures development, while the far-wake flow region (i.e. $x/c > 0.164$) is mostly dominated by modal CFI development (as further discussed in figure 7). Furthermore, the identified streak structures develop by following a constant phase trajectory which is oriented at an angle of $\simeq 6^\circ$ towards the inboard direction with respect to the free-stream flow (i.e. the X direction). This mild tilting compares well with the angle forming between developing stationary crossflow vortices and the free-stream velocity in the same set-up at more downstream chord locations, as experimentally measured and predicted by LST (Serpieri 2018).

The standard deviation fields reported in figure 2(*d–f*) indicate that in the element vicinity the regions of higher unsteadiness are mostly located in correspondence to the identified streak structures. In particular, stronger unsteady velocity fluctuations appear at the interface between the outboard low-speed and high-speed streaks, representing a local high (mostly spanwise) shear region (Klebanoff *et al.* 1992; Kuester & White 2015; Berger & White 2020). This suggests that the near-wake disturbances onset and downstream evolution are strongly related to the wall-normal and spanwise shear layers induced by the recirculation region developing in the element's wake (figure 2(*e*), Brynjell-Rahkola *et al.* 2017; Zoppini *et al.* 2022*a*). The overall level of unsteady fluctuations reduces further downstream accompanied by the progressive weakening of the streaks structures. Additionally, as the flow structures evolve downstream of the higher-fluctuation regions locally shift in correspondence to the inboard high-speed streak. Despite the observed early rise of strong unsteady disturbances, the overall transition scenario occurring in the present case appears to be driven by a typical modal CFI breakdown, as revealed by global thermography-based imaging (not shown here for brevity). Hence, it can be expected that the unsteady fluctuations detected at the end of the imaged domain further decay downstream.

Stationary disturbance velocity profiles ($\langle\bar{u}\rangle_z$) are extracted at two representative chord locations $x_1/c = 0.154$ and $x_2/c = 0.174$ (figure 2*h*,*i*). The reduction of the disturbance profile amplitude at x_2 reflects the weakening of the streak structures at more downstream locations. In addition, the developing flow disturbances are observed to grow in size along the wall-normal direction, as their maximum value moves from $y = 0.55\bar{\delta}^*$ to $y = 1.05\bar{\delta}^*$. This effect is evident in the yz plane $\bar{u}_d$ and u' contours, and can be related to the natural thickening of the BL as well as to the development of the modal CFI downstream of $x/c = 0.164$ (Saric *et al.* 2003). Specifically, at x_1 (figure 2*b*,*e*,*h*) the velocity streaks developing in the element vicinity only affect the near-wall BL region, reaching the amplitude peak value at a wall-normal distance comparable to the element height. On the contrary, the downstream evolution of the developing structures (figure 2*c*,*f*,*i*) affects the whole BL wall-normal extent through the well-known momentum modulation associated with the CFI development (Bippes 1999; Saric *et al.* 2003). Nonetheless, the absence of a secondary lobe in the disturbance velocity profiles and the relatively low maximum amplitude of the stationary disturbances ($\langle\bar{u}\rangle_z < 0.05\bar{u}_\infty$) indicate a largely linear evolution of CFI within the investigated domain. This is reflected in the close match between $\langle\bar{u}\rangle_z$ and the numerically computed local LST shape function for the λ_1 mode evolution (figure 2*i*).

Overall, both the $\bar{u}_d$ contours and $\langle\bar{u}\rangle_z$ profiles in figure 2 show that the streak structures developing in the near-wake region undergo an initial growth phase while decaying shortly downstream. The behaviour of the individual streaks can be quantified by extracting the streak amplitude (A_{str}), estimated as the maximum (minimum) $\bar{u}_d$ value for the high-(low-)speed streaks, respectively. The resulting A_{str} is reported in figure 3(*a*) for three Re_k configurations obtained by modifying the DRE array amplitude. Both in $Re_k = 192$ and $Re_k = 90$ cases the high-speed streaks feature an initial growth phase followed by subsequent decay which is more evident for the higher-amplitude forcing. The low-speed streak is instead showing a monotonic decay of the absolute amplitude value. Similar behaviour is seen for the lowest forcing amplitude considered (i.e. $Re_k = 21$). However, the measurement accuracy in this case is hindered by the overall weaker amplitude values, therefore this configuration is disregarded in the remainder of this work.

In addition to the localized amplitude estimations, a relative streak amplitude metric is defined as $A_{And} = 0.5 \times (\max(\bar{u}_d) - \min(\bar{u}_d))$ based on the criterion introduced by Andersson *et al.* (2001). The resulting estimation is reported in figure 3(*b*) and shows that

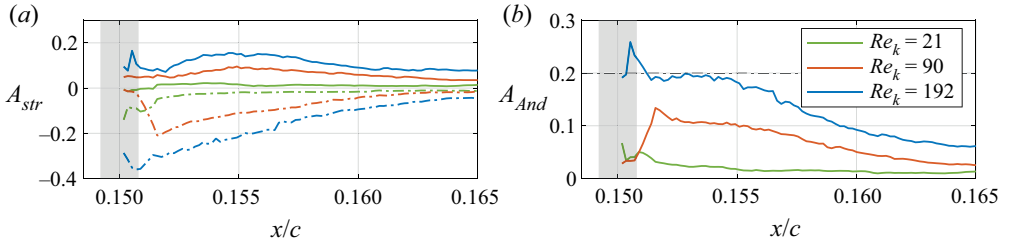

Figure 3. Streak amplitude analysis for varying Re_k: (*a*) A_{str} for high-speed (full line) and low-speed (-.) streaks; (*b*) A_{And} and amplitude limit for laminar streak breakdown (-., Andersson *et al.* 2001). Element location (shaded grey region).

the initial growth phase and subsequent decay concentrate within comparable chordwise extent for the two higher Re_k considered. Additionally, based on the A_{And} definition Andersson *et al.* identified a critical streak amplitude value of approximately $0.2\bar{u}_\infty$ as a sufficient onset condition for laminar breakdown of the developing velocity streaks in 2-D BLs. This value is not reached in the presented cases, in agreement with the laminar evolution of the flow structures observed in figure 2 and confirming the Re_k predictions. Nonetheless, the relatively high initial amplitude of the induced near-wake disturbances (especially in case $Re_k = 192$) can lead to increased unsteadiness and enhanced shear layer development in the element near-wake flow, as shown in figure 2(*e*).

Capitalizing on the volumetric information, the application of vortex identification criteria to the measured flow field allows for the characterization of the 3-D coherent structures dominating the near-element flow evolution. Specifically, in the current analysis the Q-criterion (Hunt *et al.* 1988) is applied to the time-averaged velocity field as described in § 2.3. The identified coherent structures are projected on the vortex-aligned coordinate frame (x_R, y_R, z_R) and represented in figure 4 by a positive (i.e. $Q = 0.005$, red) and a negative (i.e. $Q = -0.01$, blue) Q-criterion iso-surface. As outlined before, the near-wake flow development of each DRE is dominated by strong spanwise and wall-normal shear layers initiated by the recirculating flow region located aft of the element, identified by the green $\bar{u}_R = 0$ iso-surface in figure 4(*a*). Accordingly, the flow region corresponding to the low-speed element wake is characterized by negative values of the Q-criterion in figure 4(*a*). Conversely, the positive iso-surface identifies two coherent flow structures developing on the high-shear sides of the low-speed element's wake. These structures develop in correspondence to the positive streamwise vorticity regions and correlate well with the development of the vortical systems wrapping around and developing aft of each DRE as well as with the formation of the high-/low-speed streaks alternation.

Specifically, Kurz & Kloker (2016) describe two vortical systems forming in the element vicinity: an HSV originating from the element's sides and an inner vortex pair (IV) arising in correspondence to the element's low-speed wake. In both vortex systems, only the leg conforming to the crossflow direction of rotation (i.e. co-crossflow leg) is supported by the base flow, the other leg decaying shortly downstream. Accordingly, the two coherent structures identified by the presented Q-criterion iso-surface correspond well to the sustained co-crossflow HSV and IV legs. Further downstream of the inboard leg likely develops into a crossflow vortex, while the outboard structure appears to decay towards the downstream end of the imaged domain. The counter-crossflow HSV and IV legs described by Kurz & Kloker (2016) are not identified by the current Q-criterion application possibly due to their lower intensity and rapid decay.

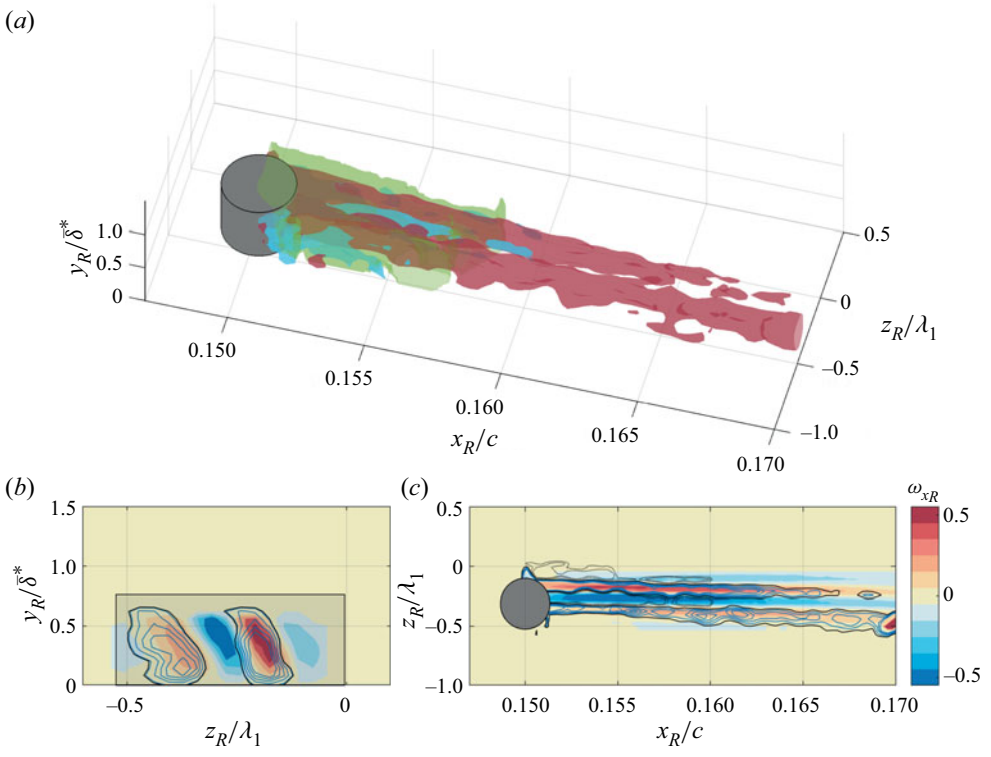

Figure 4. (*a*) The Q-criterion iso-surfaces $Q = 0.005$ (red) and $Q = -0.01$ (blue) for $Re_k = 192$ case; $\bar{u}_R = 0$ iso-surface (green). Streamwise vorticity contours and Q-criterion iso-lines in (*b*) $y_R z_R$ plane at $x/c = 0.16$ and (*c*) $x_R z_R$ plane at $y/\bar{\delta}^* = 0.55$. Full blue lines $Q > 0$ levels (5 between 0.005, 0.01), full black line $Q = 0.005$ level, grey dash-dot lines $Q < 0$ levels (5 between −0.001, −0.01).

Towards confirming the observed flow features, iso-lines of the Q-criterion in the $y_R z_R$ and $x_R z_R$ planes are reported in figure 4(*b*,*c*), extracted at $x/c = 0.16$ and $y/\bar{\delta}^* = 0.55$, respectively. The flow region surrounding the low-speed wake of the DRE is characterized by the development of the identified co-crossflow HSV and IV legs, as shown by the spatial organization of the $Q > 0$ isolines. Additionally, the streamwise vorticity contours reported in figure 4(*b*,*c*) confirm that the two iso-surfaces describe co-rotating structures corresponding well to the co-crossflow HSV and IV legs. Finally, the $Q > 0$ iso-lines as well as the chordwise evolution of the streamwise velocity contours confirm that the outboard structure decays while the inboard leg persists up to the domain end.

The results discussed so far characterize the near-wake stationary flow topology, however, they offer little insight regarding the observed growth and subsequent decay of the identified streak structures. To further investigate this aspect a spatial spectral analysis of the time-averaged spanwise velocity signal is presented hereafter, outlining the chordwise evolution of the individual Fourier modes.

3.2. *Spectral analysis and transient growth identification*

To investigate the spectral composition of the near-element flow development and to identify the dominant instability modes and their evolution, a spatial FFT in the spanwise direction (i.e. z, § 2.3) is applied to the time-averaged velocity components.

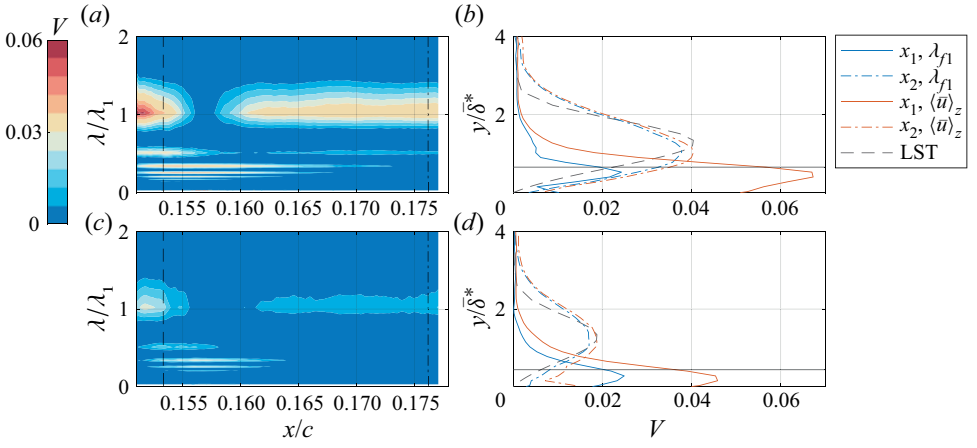

Figure 5. Spanwise FFT analysis for (*a*,*b*) $Re_k = 192$ and (*c*,*d*) $Re_k = 90$. (*a*,*c*) FFT spectra in the $x\lambda$ plane; (*b*,*d*) $\langle\bar{u}\rangle_z$ profiles and λ_{f1} FFT shape function at x_1 (dashed vertical line in *a*,*c*) and x_2 (dash-dot vertical line in *a*,*c*). The LST λ_1 shape function (- -) scaled to match $\langle\bar{u}\rangle_z$ maximum; element height (horizontal full line). Here, V stands for $\mathrm{FFT}_z(\bar{u})/\bar{u}_\infty$.

The spatial spectra development in the $x\lambda$ plane extracted at the wall-normal location of the disturbance maximum in the near-wake region (namely the maximum of $\langle\bar{u}\rangle_z$ at x_1, i.e. $y/\bar{\delta}^* = 0.55$) for $Re_k = 192$ and $Re_k = 90$, are reported in figure 5(*a*,*c*).

In both considered cases, high spectral energy is contained in the forced mode $\lambda_{f1} = \lambda_1$ both in the near-wake and in the far-wake flow region. However, in the near-wake region (i.e. at x_1) the spectral energy appears to be distributed among a wide range of higher harmonics (i.e. smaller wavelengths defined as $\lambda_{fi} = \lambda_{f1}/i$). This effect can be related to the highly localized velocity deficit region developing in the element's wake, which acts as a pseudo-pulse containing all spatial frequencies. Thus, the geometrical constraints given by the finite diameter of the DRE and their inter-spacing (i.e. d and λ_{f1}) drive the spectral energy distribution among a wide set of harmonic modes to properly describe the near-wake flow features (Zoppini *et al.* 2022*b*). The identified spectral components do not necessarily correspond to natural modal instabilities (i.e. eigensolutions to the disturbance equations), nonetheless, they are fundamental to representing the near-wake development in the modal FFT space. Accordingly, the harmonics of the dominant stationary mode achieve comparable or even higher spectral peaks in the element vicinity (figure 5*a*,*c*). As an example, for $Re_k = 192$ up to 56 % of the total disturbance energy is contained by the dominant mode and its first four harmonics. Further downstream at x_2, the λ_{f1} mode is dominating the far-wake development, only accompanied by weak λ_{f2} and λ_{f3} modes reflecting the typical traits of linear CFI modal evolution.

The behaviour of individual FFT modes is further outlined by considering the dominant features of the λ_{f1} mode shape function compared with the disturbance velocity profile $\langle\bar{u}\rangle_z$ (figure 5*b*,*d*). At x_1, the $\langle\bar{u}\rangle_z$ profile reaches significantly higher peak amplitude values than the λ_{f1} shape function, confirming the significant contribution of the higher harmonics to the near-wake flow development. However, as previously observed, the disturbances' evolution is confined within the BL region closer to the wall. Accordingly, the $\langle\bar{u}\rangle_z$ and λ_{f1} shape function peak is reached at a wall-normal distance comparable to the DRE height. This location corresponds well to the maximum fluctuation loci typically identified in the wake of isolated DRE (Klebanoff *et al.* 1992; Berger & White 2020; Zoppini *et al.* 2022*a*). Nonetheless, further downstream (i.e. at x_2) the BL development is satisfactorily

approximated by the λ_{f1} mode, as shown by the amplitude and shape match of the two profiles. Such behaviour is indicative of the onset and growth of modal CFI, as is confirmed by the similarities between $\langle\bar{u}\rangle_z$ and the λ_1 mode shape function extracted from the local LST solution (figure 5(*b*,*d*), Mack 1984; Serpieri 2018). This agreement further suggests that nonlinear interactions have a limited effect on the modal CFI development within the acquired domain.

The total disturbance amplitude ($A_{int}(\bar{u})$) and disturbance energy ($E(\bar{\boldsymbol{u}})$) as well as the amplitude ($A_{int,\lambda_{fi}}(\bar{u})$) and disturbance energy ($E_{\lambda_{fi}}(\bar{\boldsymbol{u}})$) of individual FFT modes are estimated as described in § 2.4. The chordwise evolution of the extracted amplitude and energy is reported in figure 6 for cases $Re_k = 192$ and $Re_k = 90$. Overall, the amplitude and energy evolution is similar, however, both quantities are presented at this stage as they will be the subject of independent analysis in the remainder of the work. After the initial peak and decay due to the presence of the low-momentum region in the element's wake, the total disturbance evolution undergoes mild amplitude (energy) variations in the element vicinity. However, the amplitude of the dominant λ_{f1} mode rapidly decays in the near-wake region, recovering values comparable to $A_{int}(\bar{u})$ further downstream. The observed energy recovery can be traced back to the inherently unstable nature of the primary stationary mode, which in this 3-D BL scenario should be continuously growing up to and beyond the downstream domain end according to LST (Mack 1984; Serpieri 2018). In the near wake, the harmonic λ_{f2} mode follows the primary stationary mode trend, albeit retaining lower-amplitude values up to the domain end. On the contrary, the higher harmonics reported (i.e. λ_{f3}, λ_{f4}, λ_{f5} and λ_{f6}) all show a mild amplitude growth in the range $x/c = 0.151$–0.16 before decaying further downstream. The behaviour of the individual FFT modes combined with the almost invariant total disturbance amplitude evolution indicates the presence of stationary transient mechanisms which, despite the mild amplitude variations they induce, actively condition the near-wake flow development (Landahl 1980; White *et al.* 2005; Tempelmann *et al.* 2012*a*; Zoppini *et al.* 2022*b*). In fact, as discussed later, the occurrence of transient growth mechanisms can lead to rapid initial growth of the near-wake instabilities, enhancing the CFI onset amplitude and initiating them in the far-wake region. In turn, the onset conditions impact the downstream evolution and eventual breakdown of CFI, as widely discussed in Saric *et al.* (2003). Additionally, these aspects can further explain the inability of simply linear and modal solvers to accurately describe the BL receptivity to DRE, possibly providing the necessary insights to improve these predictions. White *et al.* (2005) in their investigation dedicated to a non-swept BL already outlined that non-modal mechanisms, and in particular transient growth, are fundamental features of the near-wake flow development. Despite the reduced chordwise extent of the development of the transient mechanisms in the present set-up, namely 1.5 % chord (i.e. $\simeq 9.5d$), the evolution of the individual FFT modes is strongly comparable to the results of White *et al.* (2005). The λ_{f1} and λ_{f2} modes rapidly decay while the growth of modes λ_{f3} and λ_{f4} appear to sustain the total disturbance amplitude, thus driving the transient process.

Past theoretical works (Landahl 1980; Breuer & Kuraishi 1994; Corbett & Bottaro 2001) showed that BLs dominated by instabilities in the form of streak structures can be subject to transient growth mechanisms. These can lead to rapid initial growth of the near-wake instabilities, enhancing the CFI onset amplitude and downstream development that then follows an exponential growth process. In the present case, the occurring transient growth mechanisms are not sufficiently strong to induce the $A_{int}(\bar{u})$ growth. Nonetheless, the stationary transient disturbances appear to actively dominate and condition the near-wake flow, while the modal CFI onset occurs at a finite distance from the element. Hence, a

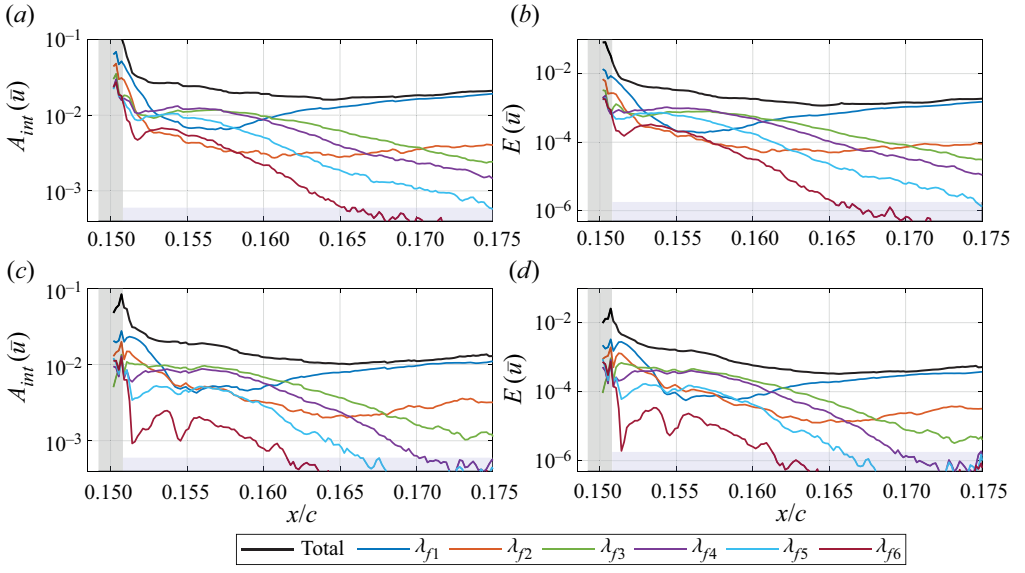

Figure 6. (a,c) Values of $A_{int}(\bar{u})$ and (b,d) $E(\bar{\boldsymbol{u}})$ for the total disturbance field and for the $\lambda_{f1} - \lambda_{f6}$ FFT harmonics for forcing cases (a,b) $Re_k = 192$; (c,d) $Re_k = 90$. Element location (grey shaded region); PTV uncertainty (blue shaded region).

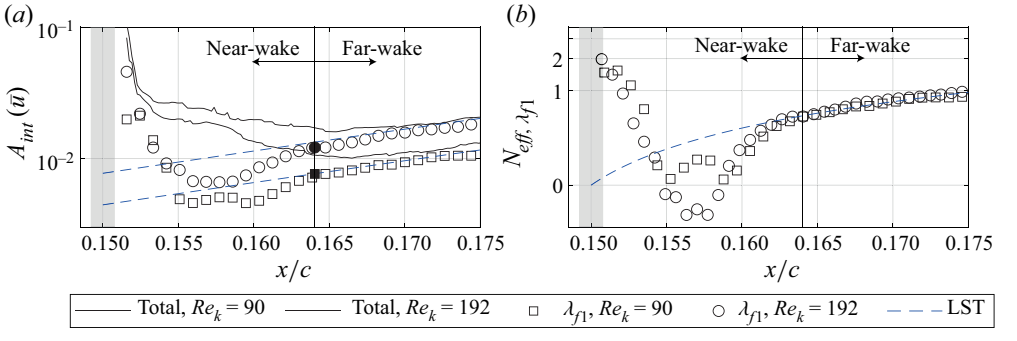

Figure 7. The A_{int} and N_{eff} estimations for the experimental FFT λ_{f1} mode (symbols) and for the LST solution λ_1 mode (solid lines). A_0 shown by filled black markers.

modal framework such as that provided by the LST method is not sufficient to thoroughly characterize the near-wake evolution.

Based on these considerations, the disturbance amplitude downstream of the initial transient growth phase can be considered as an approximation of the initial amplitude for the modal CFI growth (i.e. A_0). More specifically, the primary stationary mode amplitude ($A_{int,\lambda_{f1}}$) compared with the total disturbance amplitude evolution (figures 6 and 7a) indicates that the effect of the transient growth is limited to the near-wake flow region. In particular, aft of $x/c \simeq 0.164$ the primary stationary CFI (i.e. λ_{f1}) contains more than 80 % of the total disturbance energy, thus being representative for the modal development of the total disturbance. Therefore, the $A_{int,\lambda_{f1}}$ value at $x/c \simeq 0.164$ is considered to be representative of the λ_{f1} mode onset amplitude (A_0, black full marker in figure 7a), as confirmed by the exponential (i.e. modal) growth of the CFI further downstream.

The resulting A_0 estimations for cases $Re_k = 192$ and 90 are respectively $A_0 \simeq 0.012\bar{u}_\infty$ and $A_0 \simeq 0.008\bar{u}_\infty$.

Based on the extracted A_0 values, the experimental effective N-factor (Saric *et al.* 2019) can be defined as $N_{eff} = \ln(A_{int,\lambda_{f1}}/A_0)$. The classical N_{eff} definition proposed by Saric *et al.* (2019) considers the amplitude of the disturbances at the DRE location as the reference amplitude. However, in this work N_{eff} is computed based on the A_0 extracted at the first location where the disturbances are found to grow exponentially (i.e. $x/c = 0.164$). Figure 7(*b*) compares the experimental and LST (N_{LST}, Mack 1984; Serpieri 2018) effective N-factor evolutions. For the purpose of this comparison, all the obtained N_{eff} are offset such that $N_{LST}(x_{DRE}/c) = 0$. This procedure allows for the extraction of the N-factor values starting from the x_{DRE} location. In agreement with the observed $A_{int,\lambda_{f1}}$ trend, the experimental N_{eff} undergoes an initial decay followed by rapid growth. Further downstream, the experimental and numerical N_{eff} curves collapse, confirming the exponential growth of the CFI downstream of $x/c = 0.164$. This behaviour suggests that linear stability solutions can provide a good approximation of the initial linear phases of development of CFI granted that the onset amplitude A_0 is known downstream of the near-wake transient growth region. Specifically, for the considered case the A_0 estimate 1.4 % (i.e. 9*d*) downstream of the element location provides a satisfactory prediction. The numerical amplitude evolution can then be computed as $A_{LST} = A_0\, e^{N_{LST}}$ and is reported in figure 7(*a*), collapsing well on the experimental amplitude trends downstream of the transient growth phase. The upstream extrapolation of the LST amplitude estimation to the DRE location in figure 7(*a*) reveals the inability of fully modal assumptions to accurately predict the CFI receptivity to surface roughness (Zoppini *et al.* 2022*b*). This further highlights the importance of non-modal/transient effects in the near-wake region development, as these effectively define the A_0 value based on both the forcing geometry (mostly represented by λ_f and d) and the local BL characteristics (i.e. Re_k).

In conclusion, the FFT analysis discussed beforehand suggests that transient and non-modal mechanisms are driving the near-wake flow evolution, conditioning the onset of the emerging modal CFI. A transient growth process can be described as the combination of two signature features, i.e. an initial algebraic growth followed by an exponential decay of the developing disturbances. Therefore, to confirm the nature of the identified transient mechanisms and how these condition the CFI onset, further efforts have been dedicated to the identification of these features in the experimental disturbance energy development.

3.3. *Algebraic growth in disturbance energy and scalability*

To further characterize the nature of the stationary transient growth identified in the near-element flow, the modal disturbance energy evolution is investigated. Throughout the following discussion various Re_k cases are considered, obtained by modifying the element amplitude (cases $Re_k = 90$ and $Re_k = 192$ considered beforehand) or varying the free-stream Reynolds number for a fixed element height (cases $Re_k = 100$, $Re_c = 1.35 \times 10^6$ and $Re_k = 153$, $Re_c = 1.85 \times 10^6$ featuring k_3 elements). In all cases the forcing wavelength is kept constant at $\lambda_{f1} = \lambda_1 = 8$ mm.

As shown in figure 6, the FFT dominant stationary mode undergoes a decay–growth pattern, while modes $\lambda_{f3} - \lambda_{f6}$ follow an evident growth–decay pattern indicative of the transient mechanism occurring in the near-wake flow region. The modal disturbance energy (defined as the wall-normal integral of streamwise kinetic energy per individual FFT mode, § 2.4) is reported in figure 8(*b–e*) for modes $\lambda_{f3} - \lambda_{f6}$ at the different Re_k considered. The observed energy development confirms that these modes initially grow in

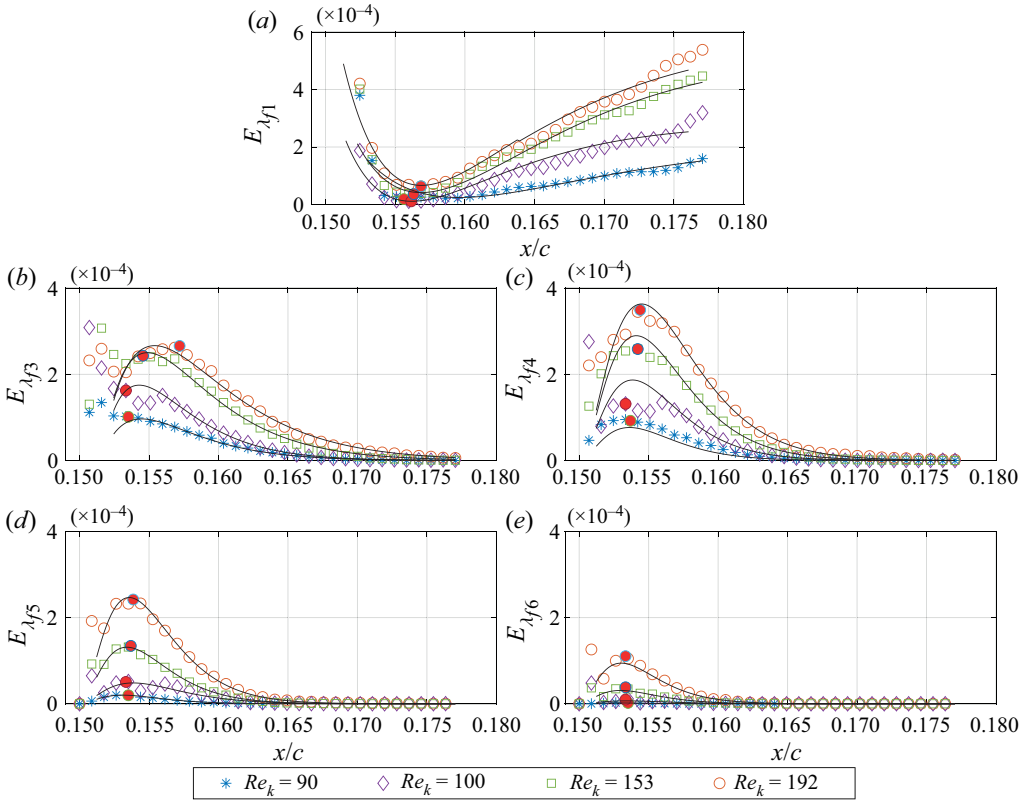

Figure 8. The $E_{\lambda_{fi}}(\tilde{\boldsymbol{u}})$ trends (symbols, 1 out of 5 shown) and maximum values (red circle) and transient growth modelling functions (black lines, White *et al.* 2005) at various Re_k for individual FFT modes; (*a*) λ_{f1}, (*b*) λ_{f3}, (*c*) λ_{f4}, (*d*) λ_{f5}, (*e*) λ_{f6}.

the element near wake, each reaching a maximum value (indicated as the red marker) and decaying further downstream. Both the maximum energy value and its distance from the element (x_{max}) depend on Re_k, while the overall chordwise extent of the transient behaviour reduces for decreasing modal wavelengths.

To further describe the growth and decay of the λ_{f3} and λ_{f4} FFT modes, White *et al.* (2005) proposed two transient growth model functions following the work by Böberg & Brösa (1988). Specifically, the two functions encompass the description of the initial algebraic growth and the exponential decay trends as follows:

$$E_{\lambda_{f3}} = a_3(x - x_{DRE})\exp(-(x - x_{DRE})/b_3) \quad \text{with } b_3 = (x_{max} - x_{DRE}) \tag{3.1}$$

and

$$E_{\lambda_{f4}} = a_4(x - x_{DRE})^2\exp(-(x - x_{DRE})/b_4) \quad \text{with } b_4 = 0.5(x_{max} - x_{DRE}). \tag{3.2}$$

In these models, coefficients a_3 and a_4 account for the algebraic growth rate as well as for the disturbance energy scaling with Re_k. Coefficients b_3 and b_4 instead are representative of the exponential decay and directly relate to the chordwise extent of the transient region. In particular, the latter coefficients can be associated with the location of the corresponding mode energy maximum (x_{max}), as indicated in (3.1) and (3.2). The evolution of the disturbance energy pertaining to λ_{f3} follows a faster growth in the immediate vicinity

of the element, while displaying a broader peak with respect to the λ_{f4} modal energy evolution. As such, the λ_{f3} energy is described by a linear dependence on the chordwise distance from the element (3.1), while the λ_{f4} energy follows a quadratic dependence on x/c (3.2). The latter model function is applied to describe the energy evolution of modes λ_{f5} and λ_{f6} as well. To fit the transient growth model functions to the experimental energy trends, only the data acquired downstream of $x/c = 0.151$ are considered to exclude the initial steep amplitude decay observed immediately aft of the element. The resulting fitted curves for the modelling of the energy transient evolution are reported in figure 8(*b–e*) as full black lines.

Despite being designed to describe stationary transient disturbances in a 2-D BL, the proposed modelling functions satisfactorily represent the λ_{f3} and λ_{f4} modal energy evolution in the considered 3-D BL case. The initial algebraic growth of λ_{f3} (figure 8*b*) is correctly captured by the linear model function, despite mild offset of the maximum location. The following exponential decay is also well modelled and shows once more that the extent of the transient behaviour is comparable throughout the different Re_k considered. Satisfactory matching is obtained for the λ_{f4} modal energy evolution (figure 8*c*), even if the peak value is mildly overestimated for the higher Re_k cases. The model function confirms that the modal energy trend associated with modes λ_{f5} and λ_{f6} follows an initial algebraic growth and exponential decay as well (figure 8*d*,*e*). The solid match observed between the quadratic–exponential fit and the energy evolution of modes $\lambda_{f4} - \lambda_{f6}$ reflects the quadratic dependence of the energy on x/c, coming from its definition in § 2.3. The fact that the behaviour of the λ_{f3} modal energy is better approximated by the linear–exponential model outlines the importance of the receptivity process and its sensitivity to the external forcing geometry in conditioning the evolution of individual FFT modes (Choudhari & Fischer 2005; White *et al.* 2005).

Differently from the 2-D BL scenario investigated by White *et al.* (2005), in the 3-D BL considered in this work the primary stationary mode λ_{f1} is inherently unstable (LST and experimental measurements, Serpieri 2018). Therefore, this mode undergoes an initial energy decay in the near-wake region in correspondence to the harmonics energy growth region while it grows further downstream (figures 6 and 8*a*). Furthermore, the characterization of the CFI initial amplitude (figure 7) showed that the λ_{f1} mode rapidly recovers to exponential growth downstream of the transient growth region occurring in the element near wake. Given these considerations, the initial decay and subsequent growth of λ_{f1} in the element vicinity can be regarded as composed of a linear algebraic decay followed by exponential growth. Figure 8(*a*) shows that the experimental disturbance energy development is well approximated by the transient growth model function of (3.1) also for the λ_{f1} mode if the sign of the a coefficient is inverted. As such, the energy evolution of the primary stationary mode describes a negative (i.e. opposite) transient growth process which conditions both the near-wake evolution and the receptivity of critical amplitude DRE. Within this work, this energy evolution is indicated as transient decay to express its direct opposition to the traditional transient growth process. This behaviour correlates well with the wake relaxation process described by Ergin & White (2006) in 2-D BL scenarios. Specifically, they identified the transient evolution of the steady instabilities to drive the near wake towards a more stable state prior to the onset of modal instabilities. However, in the 3-D BL scenario considered in the presented work, the base flow is inherently unstable to CFI, hence the wake relaxation is rapidly followed by the onset and growth of modal CFI independently of the amplitude value reached by the decaying instabilities. Nonetheless, the λ_{f1} transient decay fundamentally conditions the onset amplitude of the modal CFI, influencing their modal growth further downstream,

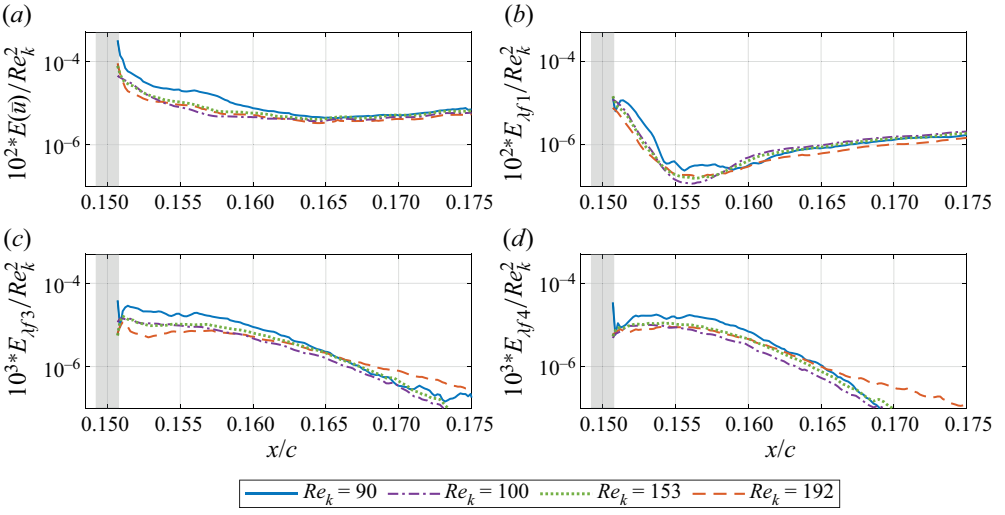

Figure 9. Variation of (*a*) $E(\bar{\boldsymbol{u}})$, and $E_{\lambda_{fi}}(\bar{\boldsymbol{u}})$ computed for FFT modes (*b*) λ_{f1}, (*c*) λ_{f2} and (*d*) λ_{f3} modes at varying Re_k. Energy is scaled by Re_k^2; element location (grey shaded region).

as also discussed in § 3.2 and figure 7 and observed in previous investigations (Breuer & Kuraishi 1994; Corbett & Bottaro 2001; Lucas 2014).

In their investigation White *et al.* (2005) identified that both a and x_{max} are well approximated by a linear dependence on Re_k. Given the mathematical composition of the considered transient growth model functions, the disturbance energy evolution is expected to scale with Re_k^2. The total disturbance energy and the energy of individual FFT modes scaled by Re_k^2 are reported in figure 9. Both the scaled total disturbance and modal energy curves almost collapse onto a single curve for the reported cases. The energy associated with the dominant mode evolution (figure 9*b*) is strongly scalable both in the transient decay region and in the far-wake flow field, where it recovers a modal behaviour and grows exponentially. Instead, the scaled energy of the harmonic FFT modes (figure 9*c*,*d*) shows comparable behaviour in the near-wake region where transient growth occurs, even if the lower Re_k considered features a mildly different evolution of the algebraic growth process. Additionally, the energy associated with the harmonic modes rapidly decays in the element far wake in agreement with the linear development of the primary stationary mode observed in the downstream flow region.

The results reported so far indicate that a transient growth mechanism driven by the primary stationary mode and its higher harmonics is dominating the near-wake evolution almost independently of the considered Re_k. Specifically, the λ_{f1} modal energy undergoes a transient decay, while the energy associated with the harmonic modes $\lambda_{f3} - \lambda_{f6}$ undergo a transient growth process. Both processes are localized within the near-wake region and feature an initial algebraic decay (growth) phase followed by exponential growth (decay) respectively. It must be noted that, given the modal energy growth characterizing the harmonics evolution and the energy decay featured by the primary stationary mode, the identified transient processes can potentially co-exist with nonlinear mechanisms. The acquired dataset, however, does not provide sufficient information to prove this hypothesis. Nonetheless, transient growth processes in 3-D BLs receptive to critical DRE need to be accounted for to correctly estimate the modal instabilities' initial amplitude and growth despite their very mild effect on the total disturbance amplitude evolution. This can be

regarded as one of the main differences between the investigated 3-D scenario and the more typical wake relaxation or bypass transition configurations widely characterized for 2-D BLs, in which the primary streak mode simply decays downstream if not strong enough to cause laminar breakdown.

Overall, the observed transient energy evolution scales well with Re_k^2. The current investigation only considers DRE of cylindrical shape, but modifications of the spanwise array wavelength (i.e. element inter-spacing) and DRE diameter appear to significantly affect the identified transient mechanisms by conditioning the modal energy distribution. In fact, the relation between the chosen element inter-spacing (i.e. λ_{f1}), setting the primary stationary mode wavelength, and the element diameter (d) conditions the range of wavelengths following an algebraic growth process (i.e. modelled by (3.2)). Specifically, for the considered critical forcing case $\lambda_{f3} \simeq 1.3d$, $\lambda_{f4} \simeq 1d$, $\lambda_{f5} \simeq 0.8d$ and $\lambda_{f6} \simeq 0.7d$. This can be related to the effect of the finite element diameter on the spatial arrangement and spacing of the HSV system (Munaro 2017), which further contributes to defining the strength of the near-wake transient growth process (Choudhari & Fischer 2005; White *et al.* 2005). Thus, the investigated parameter range has been expanded by modifying the DRE array forcing wavelength λ_{f1} to further investigate the steady transient disturbances receptivity to the forcing geometry.

3.4. *Variations of forcing wavelength*

The results discussed in § 3.3 outlined a significant dependence of the modal energy distribution and consequently of the occurring transient processes in the near wake on the geometry of the considered problem (parametrized using λ_{f1} and d). Therefore, to further investigate the effects of the external forcing configuration the receptivity of the near-wake steady transient disturbances to a modification of the forcing wavelength is explored. At this point, it must be clarified that none of the forcing cases considered in this section leads to BL transition in the element vicinity, hence they fall in the critical amplitude forcing definition. Nonetheless, to distinguish between configurations forcing at wavelength $\lambda_{f1} < \lambda_1$ and $\lambda_{f1} > \lambda_1$ the definitions of sub-critical wavelength (SBW) and super-critical wavelength (SPW) forcing are respectively used throughout the following discussion. With reference to figure 1, in the previous sections cases $Re_k = 100$, 153 and 192 have been inspected in a critical wavelength forcing configuration (i.e. forcing the most unstable mode λ_1). In the following analysis, for each of the considered Re_k a SBW ($\lambda_{f1} = \lambda_{3/2}$, Saric *et al.* 1998) and a SPW ($\lambda_{f1} = \lambda_{2/3}$) array are investigated. It should be noted that according to LST analysis the λ_1 wavelength corresponds to the most unstable mode in all considered configurations, however, modes $\lambda_{3/2}$ and $\lambda_{2/3}$ are both locally amplified at the DRE location of application.

Considering the SBW forcing case, the velocity contours reported in figure 10 show that the near-wake flow topology retains its main characteristics, albeit being dominated by a $\lambda_{3/2}$ flow periodicity. A low-speed streak develops in correspondence to each element's wake, while two high-speed streaks form on the wake's sides. The streaks evolution compares well with the critical wavelength case, as confirmed by the A_{And} estimation (figure 10*d*). Moreover, the extracted FFT spectra indicate that the near wake features high spectral energy content for the forced $\lambda_{f1} = \lambda_{3/2}$ mode and its harmonics (figure 10*e*). The spectral energy associated with harmonic modes decays further downstream, leaving a BL modulated by the development of a sub-critical CFI (Saric *et al.* 1998). The disturbance velocity profiles compare well with the λ_{f1} FFT shape function towards the downstream end of the acquired domain, while the amplitude differences observed in the near wake are attributed to the harmonics contributions (figure 10*c*).

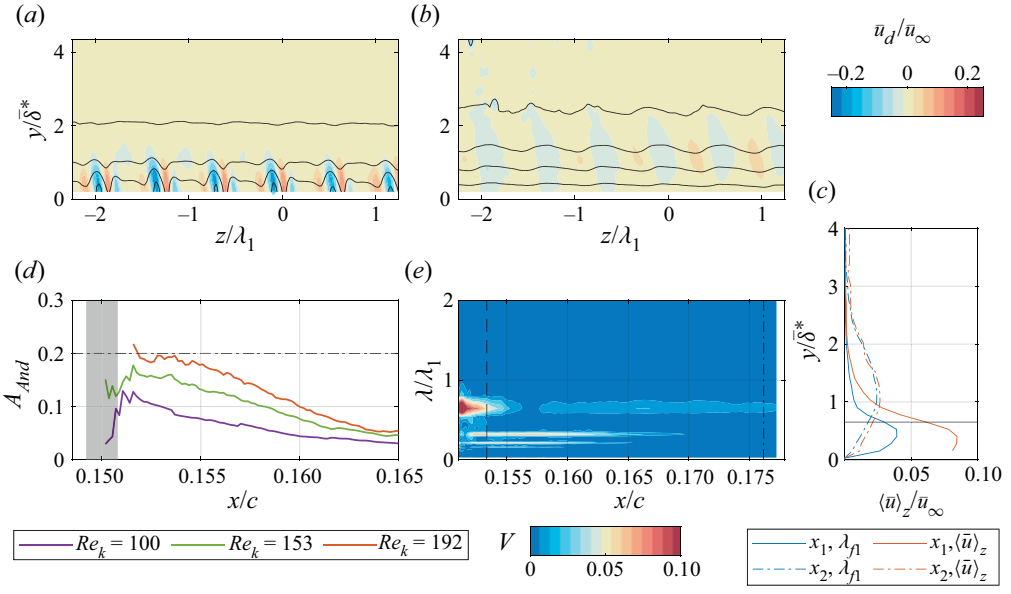

Figure 10. Stationary flow topology for forcing case $\lambda_{f1} = \lambda_{3/2}$, $Re_k = 192$ (i.e. k_3): (*a*,*b*) $\bar{u}_d$ in the yz plane at (*a*) $x_1 = 0.154c$ and (*b*) at $x_2 = 0.174c$; (*c*) $\langle\bar{u}\rangle_z$ profiles and λ_{f1} FFT shape functions at x_1 and x_2; element height (horizontal full line); (*d*) A_{And} and amplitude limit for laminar streak breakdown (-. line) for various Re_k. (*e*) Spanwise FFT spectra in the $x\lambda$ plane at $y = 0.55\bar{\delta}^*$. Here, V stands for $\mathrm{FFT}_z(\bar{u})/\bar{u}_\infty$.

The near-element flow for the SPW forcing case (not reported for the sake of brevity) is characterized by similar features as the so-far considered cases. Once more, the harmonics have an important role in the element's near wake, while rapidly decaying shortly downstream. Additionally, the $Re_k = 192$ forcing case reaches an A_{And} amplitude close to the laminar breakdown threshold identified by Andersson *et al.* (2001). Nonetheless, the streak amplitude rapid decay prevents the onset of laminar breakdown in the near-element region.

Despite the variation of the dominant flow periodicity due to the modified forcing wavelength, the near-element stationary flow topology reflects all the dominant flow features discussed for the $\lambda_{f1} = \lambda_1$ forcing case. Accordingly, stationary transient growth disturbances drive the near-wake evolution also in the SBW and SPW configurations. In particular, figure 11 shows the chordwise evolution of the total disturbance amplitude and of the amplitude of individual FFT modes (where $\lambda_{fi} = \lambda_{f1}/i$) for the two forcing wavelengths considered. In both cases the decay of the dominant mode (i.e. the forced mode λ_{f1}) combined with the evolution of the total disturbance amplitude indicate that a transient growth mechanism is driving the near-wake evolution and relaxation. Figure 6 outlined that in the $\lambda_{f1} = \lambda_1$ forcing case the evolution of stationary transient disturbances is mostly represented by the transient decay of mode λ_{f1} and the transient growth of FFT modes $\lambda_{f3} - \lambda_{f6}$ (i.e. $1.3d$–$0.7d$). However, figure 11 shows that a change of λ_{f1} leads to a redistribution of the disturbance energy associated with the individual FFT modes. More specifically, in the SBW forcing (figure 11*a*) the harmonic modes λ_{f2} and λ_{f3} undergo a strong transient growth process. Additionally, the λ_{f4} mode is only giving a mild contribution, while the higher harmonics are rapidly decaying. The SPW forcing reported in figure 11(*b*) is characterized by the decay of the first three harmonic modes (i.e. $\lambda_{f1} - \lambda_{f3}$). In this case, the transient growth behaviour appears to be only weakly

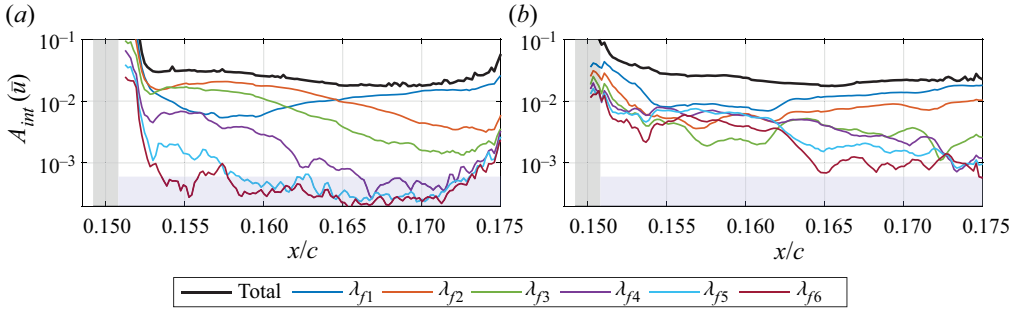

Figure 11. Values of $A_{int}(\bar{u})$ for the total disturbance field and for the $\lambda_{f1} - \lambda_{f6}$ FFT harmonics for forcing cases $Re_k = 192$ and (*a*) $\lambda_{f1} = \lambda_{3/2}$, (*b*) $\lambda_{f1} = \lambda_{2/3}$. Element location (grey shaded region); PTV uncertainty (blue shaded region).

sustained by mode λ_{f4} with more significant contributions of modes λ_{f5} and λ_{f6}. In the latter case, the larger element spanwise inter-spacing leaves the possibility of stronger modal interactions (Saric *et al.* 1998), justifying the more irregular amplitude trends observed. These observations further highlight that besides affecting the overall modal CFI development, the geometry of the external forcing tends to drive the non-modal processes and the behaviour of the instabilities also in the near-wake flow region. In fact, the energy distribution within the FFT spectra appears to favour the modes corresponding to wavelengths close to the DRE diameter. This is the case for wavelengths $\lambda_{f2} = 1.25d$ and $\lambda_{f3} = 0.8d$ in the SBW case; or for wavelengths $\lambda_{f5} = 1.1d$ and $\lambda_{f6} = 0.9d$ in the SPW scenario.

Nonetheless, the primary stationary mode appears to undergo transient decay both in the SBW and SPW forcing scenarios, almost independently from the forcing wavelength modification. This is confirmed by comparing the experimental amplitude trends with the LST prediction, as already outlined in the analysis presented in figure 7. The corresponding results are reported in figure 12 for $Re_k = 192$ and varying λ_{f1}. This comparison outlines once more that the instability evolution differs from the modal LST solution in the element vicinity, however, the experimentally computed amplitude trend follows a modal growth downstream of $x/c = 0.164$. Hence, the A_0 amplitude for the dominant (i.e. most unstable) CFI mode can be estimated at $x/c = 0.164$ also for these cases, resulting in $A_0 = 0.010\bar{u}_\infty$ and $0.011\bar{u}_\infty$ for the SBW and SCW forcing respectively. These values are slightly lower than those found for the critical forcing at comparable Re_k, reflecting the variation of the forcing geometry (i.e. the diameter and λ_{f1} ratio, Radeztsky *et al.* 1999). Nonetheless, the mild A_0 differences observed suggest that the transient growth process is mostly unaffected by the BL stability characteristics (Kurz & Kloker 2014).

Additionally, figure 13 compares the experimental energy trend associated with the forced wavelength λ_{f1} with the transient growth model function of (3.1). This analysis is presented for both SBW and SPW configurations at various Re_k. The modelled energy corresponding to the baseline case $Re_k = 192$ and $\lambda_{f1} = \lambda_1$ is also reported (black dotted line). It is apparent that the primary stationary mode undergoes transient decay in all measured cases, as confirmed by the match between the experimental energy trend and the energy model function. This indicates that within the considered critical amplitude range, the transient decay experienced by the primary stationary mode occurs independently from the chosen forcing wavelength and can be satisfactorily modelled by using (3.1) and inverting the sign of the a coefficient. This provides a reliable approximation of the modal CFI onset amplitude and location as discussed for the critical forcing case (§ 3.2).

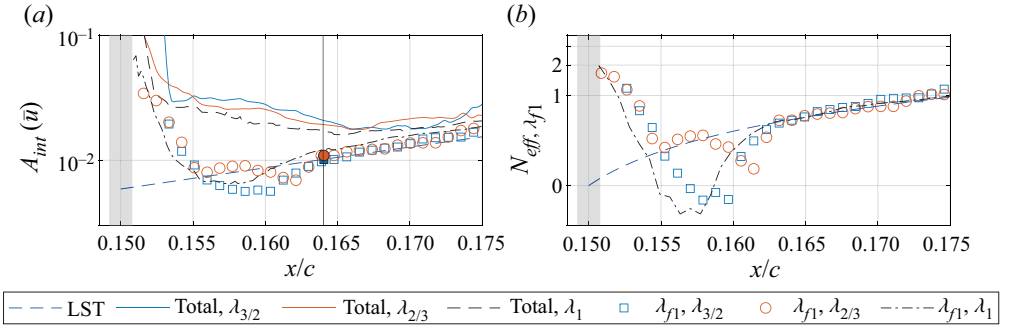

Figure 12. The A_{int} and N_{eff} estimations for the experimental FFT λ_{f1} mode (symbols) for cases $\lambda_{f1} = \lambda_{3/2}$ and $\lambda_{2/3}$ at $Re_k = 192$ and for the LST solution λ_1 mode (solid lines). Here, A_0 shown by filled coloured markers.

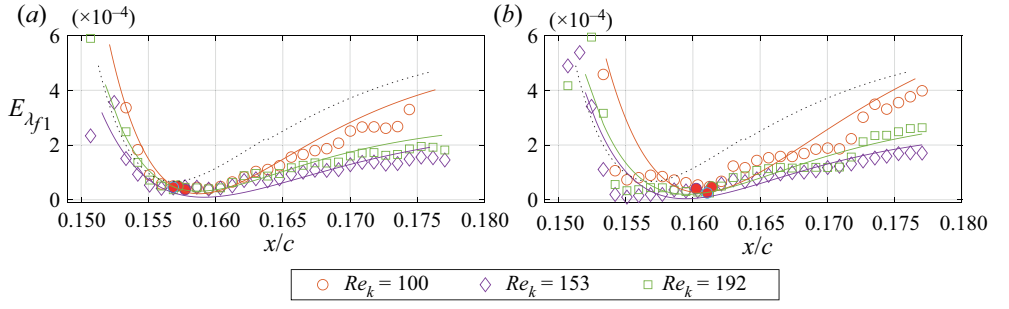

Figure 13. The $E_{\lambda_{f1}}(\bar{u})$ trends (symbols, 1 out of 5 shown) and minimum values (red circle), and transient growth modelling functions (full lines, White *et al.* 2005) at various Re_k for (*a*) $\lambda_{f1} = \lambda_{3/2}$ and (*b*) $\lambda_{f1} = \lambda_{2/3}$. Energy modelling function for $Re_k = 192$, $\lambda_{f1} = \lambda_1$ (black dotted line).

Furthermore, the forced mode (i.e. primary stationary mode) energy evolution obtained in the critical wavelength forcing case appears to undergo steeper decay and faster growth than for the non-critical cases considered. This agrees well with the idea that the λ_{f1} mode energy growth in this 3-D boundary layer scenario is driven by the inherently unstable nature of the forced mode.

For each of the considered forcing wavelengths, the energy distribution among the individual FFT modes is robust to Re_k modifications. This is evident in figure 14, reporting the evolution of the total disturbance energy and the modal energy scaled by Re_k^2 for the various forcing wavelengths considered. The scaled total energy collapses on a single curve for the super-critical and critical forcing (black dash-dot line), while it follows a mildly different growth process in the near-wake region for the SBW forcing case. The λ_{f1} mode chordwise evolution scales well with Re_k^2, confirming the dominant mode initial decay and downstream exponential growth are common traits to all of the considered forcing configurations. Given the dependence of the modal energy distribution on λ_{f1} and d, the scaling of the higher harmonics collapses on a different curve for each forcing wavelength considered.

The presented analysis indicates that, independently of the chosen λ_{f1}, the evolution of the primary stationary mode and its harmonics in the near-wake region is strongly affected by the presence of transient growth mechanisms, driving the near-wake relaxation through two different scenarios. On the one hand, the primary stationary mode appears to follow a

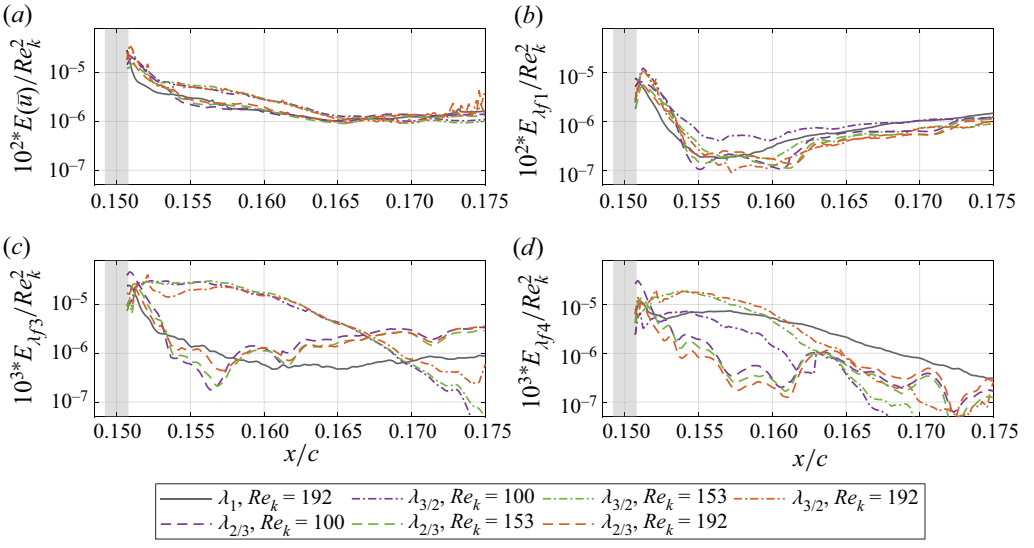

Figure 14. Variation $E(\bar{\boldsymbol{u}})$ for (*a*) total disturbance field, (*b*) FFT λ_{f1}, (*c*) λ_{f2} and (*d*) λ_{f3} modes at varying Re_k and λ_{f1}. Energy is scaled by Re_k^2; element location (grey shaded region).

transient decay process, recovering from an initial algebraic decay into exponential energy growth. This is in agreement with the inherent instability of the primary stationary mode, which according to LST grows modally along the wing chord. On the other hand, a sub-set of the higher harmonic modes undergoes a more traditional transient growth process in the near-wake region. The external forcing geometry, mostly represented by the combination of the λ_f and d, significantly affects the modal energy distribution within the FFT spectra, thus selecting the set of harmonics and the strength of the transient growth process.

4. Super-critical near-element flow

The analysis of the near-element stationary flow indicates that transient growth is a fundamental mechanism for the near-wake flow evolution. Nevertheless, none of the cases considered in the previous sections features forcing amplitudes leading to bypass transition (i.e. BL transition in the element vicinity). Therefore, the last part of the presented work is dedicated to the investigation of forcing configurations associated with super-critical behaviour, i.e. flow tripping, outlining the corresponding near-element flow topology and the role of the near-wake stationary transient disturbances in the transitional process. With reference to figure 1, configurations featuring $Re_k > 200$ are considered under Re_k and λ_{f1} modifications.

The critical DRE wavelength array (i.e. $\lambda_{f1} = \lambda_{f1}$) at $Re_k = 330$ is initially considered as the representative forcing case. The corresponding time-averaged disturbance velocity field ($\bar{u}_d$) is reported in figure 15(*a–c*), while figure 15(*d–f*) show the temporal fluctuation standard deviation contours (u'). The $\bar{u}_d$ contours of figure 15(*a*) indicate that the near-wake flow is dominated by the alternation of high- and low-speed streaks spatially organized as described for the previously considered critical cases (i.e. figure 2). However, for the current super-critical amplitude forcing the high-speed streaks developing on the wake's flanks rapidly merge, substituting the low-speed wake at $x/c \simeq 0.158$ (i.e. $\simeq 5d$ downstream of the element, solid vertical black line in figure 15*a*). This behaviour closely resembles the near-wake flow development of isolated DRE with super-critical

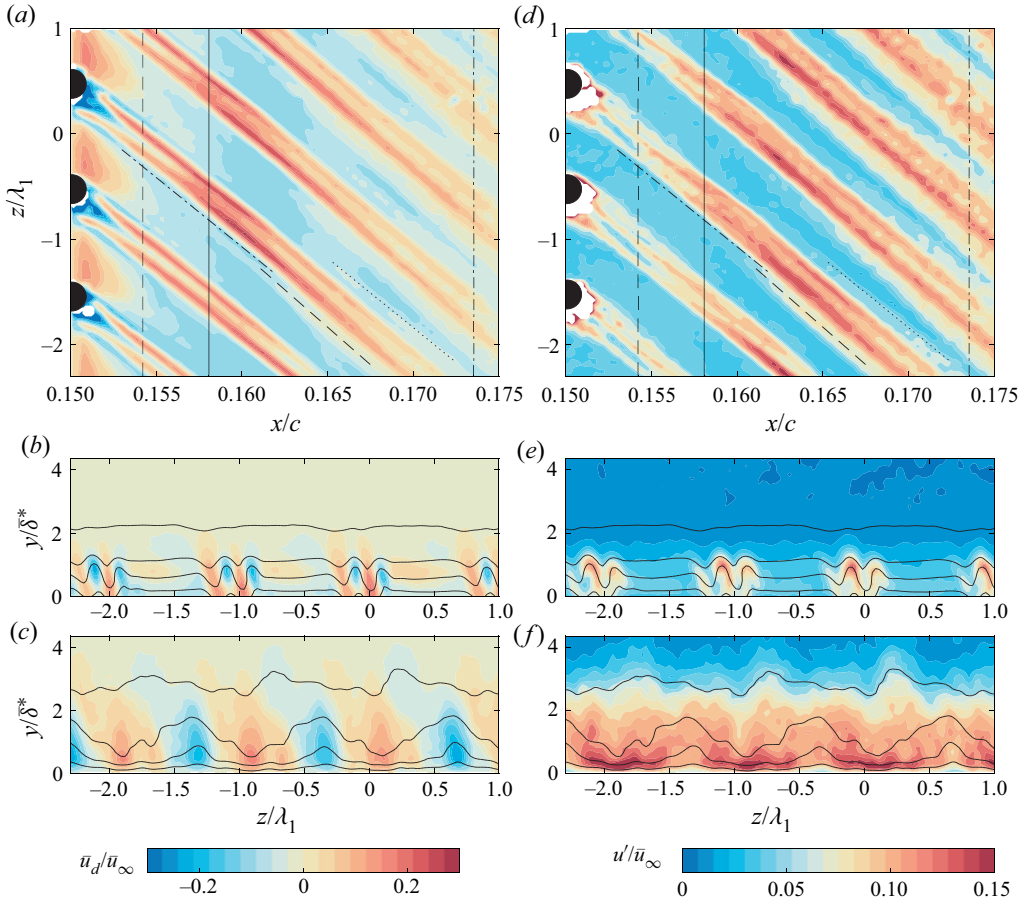

Figure 15. (*a–c*) Values of $\bar{u}_d$ and (*d–f*) u' for forcing case λ_{f1}, $Re_k = 330$ in (*a*,*d*) the xz plane at $y/\bar{\delta}^* = 0.55$; (*b*,*e*) in the yz plane at $x_1 = 0.154c$ (vertical dashed line in *a*), and (*c*,*f*) at $x_2 = 0.174c$ (vertical dash-dot line). Vertical full line in (*a*) at $x/c = 0.158$.

amplitude in 2-D and 3-D BL cases (Kendall 1981; Klebanoff *et al.* 1992; Kurz & Kloker 2016; Zoppini *et al.* 2022*a*). Additionally, the inboard and outboard high-speed streaks forming in the near-wake flow region can be identified within the merged high-speed wake. As observed for the critical amplitude elements, the inboard high-speed streak undergoes a stronger growth process while evolving downstream if compared with its outboard counterpart.

The identified merging of high-speed streaks is usually associated with the onset of turbulent flow in spatial correspondence to the element's wake (Kendall 1981; Klebanoff *et al.* 1992). This is confirmed by the increased velocity fluctuation level shown by the u' contours in figure 15(*d*). Specifically, the super-critical near wake ($x/c < 0.155$) is characterized by the development of a high-fluctuation region spatially overlapping to the low-speed streak (figure 15(*d*,*e*), Klebanoff *et al.* 1992; Loiseau *et al.* 2014). However, further downstream at the region of high-speed streak merging ($x/c \simeq 0.158$), the intensity of the velocity fluctuation increases and its spatial distribution begins to spread along the spanwise and wall-normal directions, eventually occupying the whole element's wake.

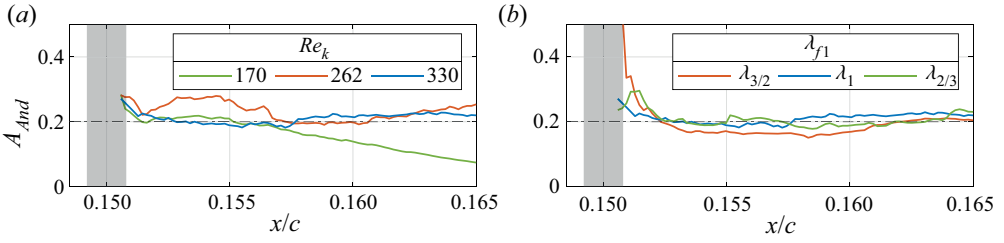

Figure 16. Value of A_{And} and amplitude limit for laminar streak breakdown (-. line) for forcing (a) at $\lambda_{f1} = \lambda_1$ varying Re_k; (b) at $Re_k = 330$ and varying λ_{f1}. Element location (grey shaded region).

Accordingly, each individual DRE wake appears to initiate a turbulent wedge (Klebanoff *et al.* 1992) at the merging location of $x/c \simeq 0.158$.

The u' contours provide additional information regarding the wedge formation and development. Specifically, the spanwise spreading of the wedge can be associated with the formation of a cascade of low- and high-speed streaks on the sides of the high-speed wake (Berger & White 2020). An inboard low-speed streak (dash-dot line in figure 15a) is initiated in the immediate vicinity of the element and grows along the inboard side of the high-speed wake. More downstream, a high-speed streak becomes evident at $x/c \simeq 0.16$ on the wake inboard side (dashed line in figure 15a), merging shortly downstream with the element's high-speed wake. A similar mechanism drives the spanwise wedge opening towards the outboard direction as shown by the high-speed streak development at $x/c \simeq 0.165$ and its downstream merging with the high-speed wake region (dot-dot line in figure 15a). The development of the identified high-speed structures leads to a localized increase in the level of the velocity fluctuation, driving the spanwise expansion of the high-fluctuation region as shown by figure 15(d). However, the role of this wedge-opening mechanism in the current configuration is limited by the flow periodicity. Specifically, the DRE inter-spacing leads to the merging of the individual turbulent wedges already towards the downstream end of the acquired domain (i.e. $x/c \simeq 0.174$). While the extent of the PTV domain is not sufficiently long to confirm this, the newly formed turbulent BL is expected to be largely homogeneous in the spanwise direction shortly downstream.

The estimation of the relative streak amplitude A_{And} clearly shows that the amplitude limit for the laminar breakdown is reached in the element vicinity (figure 16). While evolving downstream, the A_{And} values corresponding to the $Re_k = 330$ forcing case are still higher than $0.2\bar{u}_\infty$, differently than the $Re_k = 192$ case previously investigated and in agreement with the observed breakdown of the streak structures and turbulence onset. Figure 16(a) indicates that comparable behaviour is achieved for the $Re_k = 262$ forcing (obtained by reducing Re_c to 1.85×10^6), while the lower Re_k case (corresponding to $Re_c = 1.35 \times 10^6$) features A_{And} behaves critically, leading to the development of modal CFI as discussed in § 3. Despite the higher DRE amplitude considered (i.e. k_4), this behaviour agrees well with the $Re_k < 200$ threshold pertaining to critical amplitude forcing configurations. Figure 16(b) instead shows that a modification of λ_{f1} has an almost negligible effect on the A_{And} amplitude trends for $Re_k = 330$.

The observed stationary flow topology is reflected by the analysis of the Q-criterion iso-surfaces reported in figure 17. Comparably to figure 4, the strong spanwise and wall-normal shear layers dominating the near-wake flow development are identified in figure 17(a) by a negative Q iso-surface (i.e. $Q = -0.08$, blue). The coherent structures organization is instead presented by means of a positive Q-criterion iso-surface (i.e. $Q = 0.01$, red). In this super-critical scenario, three coherent flow structures are identified

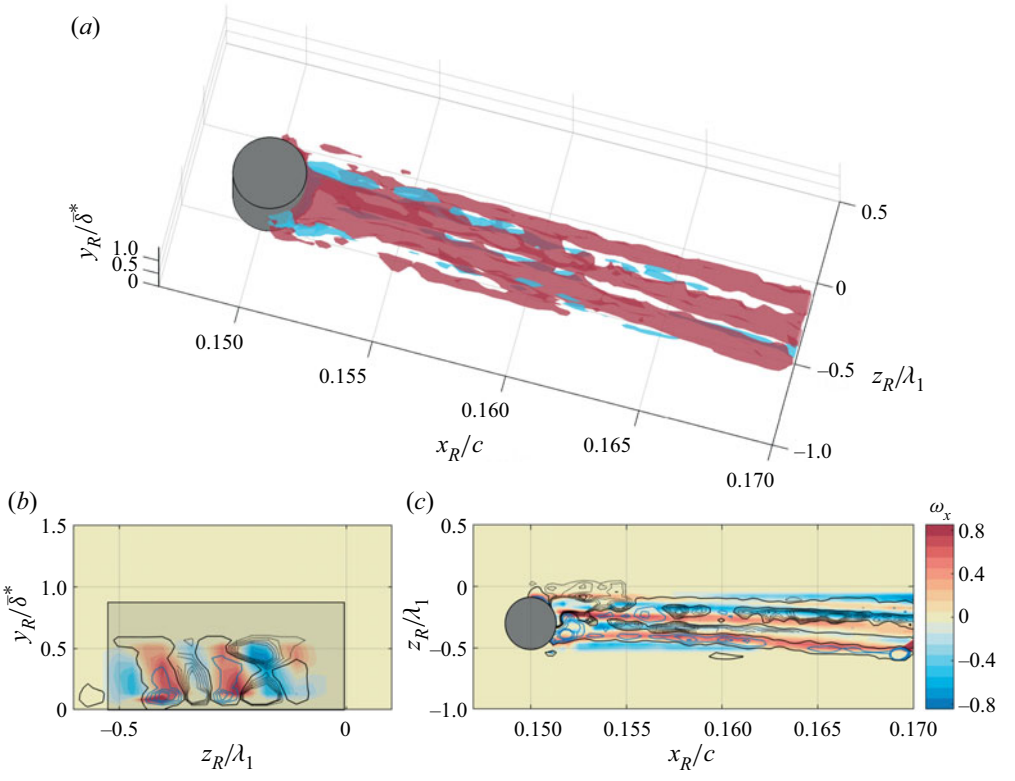

Figure 17. (*a*) The Q-criterion iso-surfaces $Q = 0.01$ (red) and $Q = -0.08$ (blue) for $Re_k = 330$ case. Streamwise vorticity contours and Q-criterion iso-lines in (*b*) $y_R z_R$ plane at $x/c = 0.157$ and (*c*) $x_R z_R$ plane at $y/\delta^* = 0.55$. Full blue lines $Q > 0$ levels (5 between 0.01, 0.1), full black line $Q = 0.01$ level, grey dash-dot lines $Q < 0$ levels (5 between -0.008, -0.01).

developing in correspondence to the low-speed element's wake and its high-shear sides. The two structures developing at the element's inboard side and in correspondence with its low-speed wake are initiated in the element vicinity, while the outboard structure originates shortly downstream of $x/c \simeq 0.155$ (i.e. shortly downstream of the super-critical DRE near-wake region). The former two structures correlate well with the development of the co-crossflow HSV and IV legs wrapping around and developing aft of each DRE (Kurz & Kloker 2016), comparably to what was observed for the critical DRE amplitude case of figure 4. On the other hand, the identified outboard structure possibly relates to the merging of the high-speed streaks, as it can contribute to the observed increase in the overall flow unsteadiness. The three structures grow and persist up to the downstream domain end, possibly merging further downstream with assistance from the breakdown-enhanced mixing. Towards confirming the observed flow features, iso-lines of the Q-criterion in the $y_R z_R$ and $x_R z_R$ plane are reported in figure 17(*b*,*c*) in combination with the streamwise vorticity contours. The ω_x contours indicate that the three coherent structures are all co-rotating. Additionally, the spatial organization of the $Q > 0$ isolines confirms that the inboard and wake structures form already in the element near wake, while the outboard structure appears further downstream.

The spatial FFT performed for the super-critical near-wake flow region compares well with the previously considered lower Re_k cases (i.e. $Re_k = 90$, 100, 153, 192), despite overall higher spectral amplitude levels (figure 18). For all the three λ_{f1} considered the

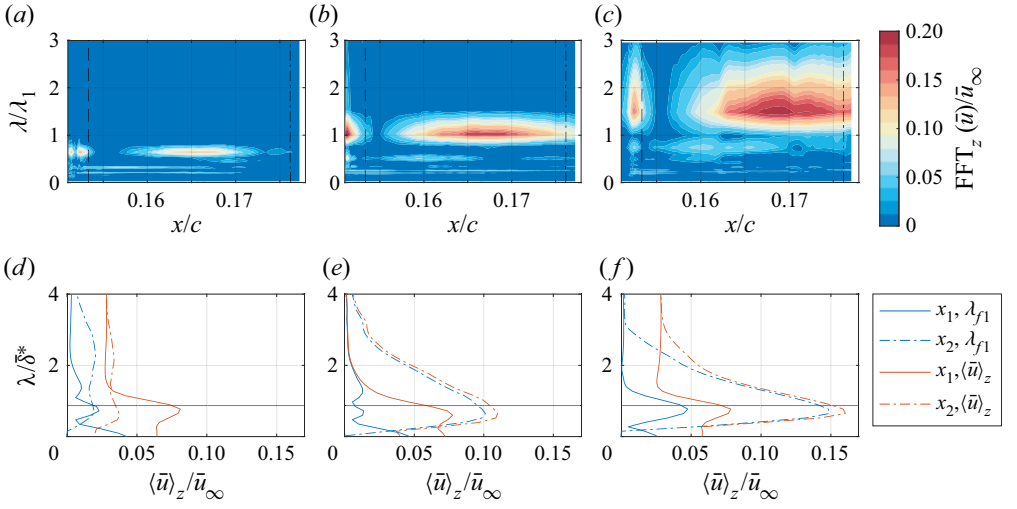

Figure 18. (*a–c*) Spanwise FFT spectra in the $x\lambda$ plane (vertical dashed line at x_1, vertical dash-dot line at x_2) and (*d–f*) $\langle\bar{u}\rangle_z$ profiles and λ_{f1} FFT shape function at x_1 and x_2 for forcing at $Re_k = 330$ and (*a*,*d*) $\lambda_{f1} = \lambda_{3/2}$; (*b*,*e*) $\lambda_{f1} = \lambda_1$; (*c*,*f*) $\lambda_{f1} = \lambda_{2/3}$; element height (horizontal full line).

forced wavelength strongly conditions the dominant flow periodicity, however, the λ_{f1} harmonics always retain high energy content in the near-wake region (figure 18*a–c*). Additionally, dominant near-wake disturbances only affect the BL in the wall vicinity as confirmed by the peak of the corresponding FFT shape functions, located approximately at the same wall-normal location as the element's top (figure 18*d–f*). Interestingly, the amplitude peak location is almost unaltered at the downstream chord location considered (x_2). This suggests that the dominant BL disturbances develop in the form of velocity streaks even downstream of the near-wake region, without evolving into modal CFI. This effect is comparable to the flow field incurred by isolated super-critical DRE in 2-D and 3-D BLs (Klebanoff *et al.* 1992; Loiseau *et al.* 2014; Zoppini *et al.* 2022*a*).

To investigate the presence of transient growth mechanisms in the near-wake flow region, the evolution of the individual FFT modes is considered. The critical amplitude forcing configurations (§ 3) proved that the FFT modes undergoing stronger transient growth are mostly sensitive to the ratio between the forcing wavelength and the diameter of the DRE. As such, the total disturbance amplitude evolution and the integral amplitude of the individual FFT modes are reported in figure 19 for the three λ_{f1} considered at $Re_k = 330$. The observed amplitude evolution is indicative of the presence of stationary transient disturbances in the near wake. However, for the three considered λ_{f1}, the primary stationary mode rapidly recovers to amplitude values comparable to the total disturbance amplitude (i.e. at $x/c \simeq 0.158$), growing further downstream. The mild decay observed in both the total amplitude and the primary stationary mode amplitude towards the end of the domain, reflects the breakdown of the laminar structures developing in the BL and the onset of turbulence (Bippes 1999).

The energy distribution within individual FFT modes and their contribution to the transient process are consistent with the previously discussed cases for the $\lambda_{f1} = \lambda_{3/2}$ forcing (figure 19*a*). Redistribution of the modal energy towards mode λ_{f2} is instead observed for the $\lambda_{f1} = \lambda_1$ and $\lambda_{f1} = \lambda_{2/3}$ forcing (figure 19*b*,*c*). This suggests that more amplified transient disturbances develop in the considered super-critical forcing scenario, driven by the λ_{f2} mode evolution as well. Nonetheless, the growth of the stationary

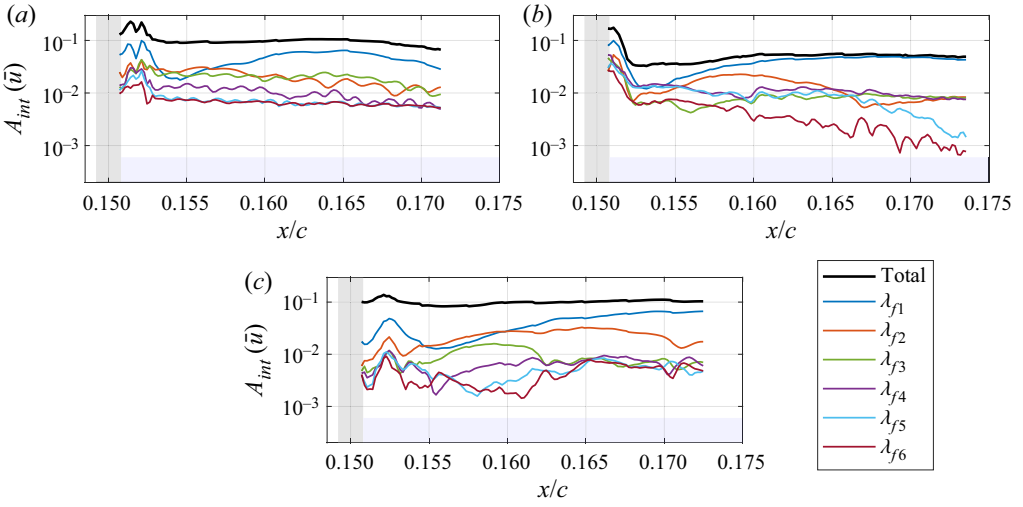

Figure 19. Value of $A_{int}(\bar{u})$ for the total disturbance field and for the $\lambda_{f1} - \lambda_{f6}$ FFT harmonics for forcing at $Re_k = 330$ and (*a*) $\lambda_{f1} = \lambda_{3/2}$, (*b*) $\lambda_{f1} = \lambda_1$, (*c*) $\lambda_{f1} = \lambda_{2/3}$. Element location (grey shaded region); PTV uncertainty (blue shaded region).

disturbances as described by the reported amplitude trends only gives a partial insight into the instabilities responsible for the observed laminar breakdown. More specifically, as indicated by the high and widespread unsteady fluctuation level, the unsteady disturbances developing in the element's wake appear to play a fundamental role in driving the turbulence onset (Klebanoff *et al.* 1992). In fact, figure 19 indicates that the rapid growth of the dominant mode occurs in the proximity of $x/c \simeq 0.158$, namely the chord location corresponding to the initiation of the inboard high-speed streak driving the spanwise spreading of the high-fluctuation region. For this super-critical amplitude scenario, the role of the primary stationary mode transient decay (and of the wake relaxation) appears to be reduced, as the onset of modal CFI is bypassed by the breakdown of the laminar structures. On the contrary, the transient growth of the harmonic modes and the geometrical characteristics of the forcing element, i.e. the diameter and amplitude of the DRE, appear to play a more relevant role. Due to the increased forcing amplitude, the near-wake flow evolution is accompanied by an overall increase of unsteady fluctuation level, indicative of the growth of unsteady wake instabilities. The combination of higher shears and harmonics transient growth in the near-wake region rapidly drives the velocity streaks growth to super-critical levels according to the model proposed by Andersson *et al.* (2001), preventing the relaxation of the near wake to a state stable to unsteady fluctuations (White *et al.* 2005). Hence, in the super-critical flow scenario the receptivity process leads to the laminar breakdown of the near-wake structures and the onset of turbulence through bypass transition, as commonly identified in previous works (e.g. Andersson *et al.* 1999; Reshotko 2001). The time-averaged nature of the conducted measurements does not allow access to unsteady disturbance frequency information. Nonetheless, the stationary near-wake flow field of the super-critical DRE appears to be comparable to that of super-critical isolated roughness elements. This is largely expected as the locality of the near wake and developing unsteady mechanisms allows for decoupling each element in a DRE array from its neighbours in the corresponding flow region. Hence, the available past studies on the unsteady near wake of isolated elements can provide preliminary insights on the nature

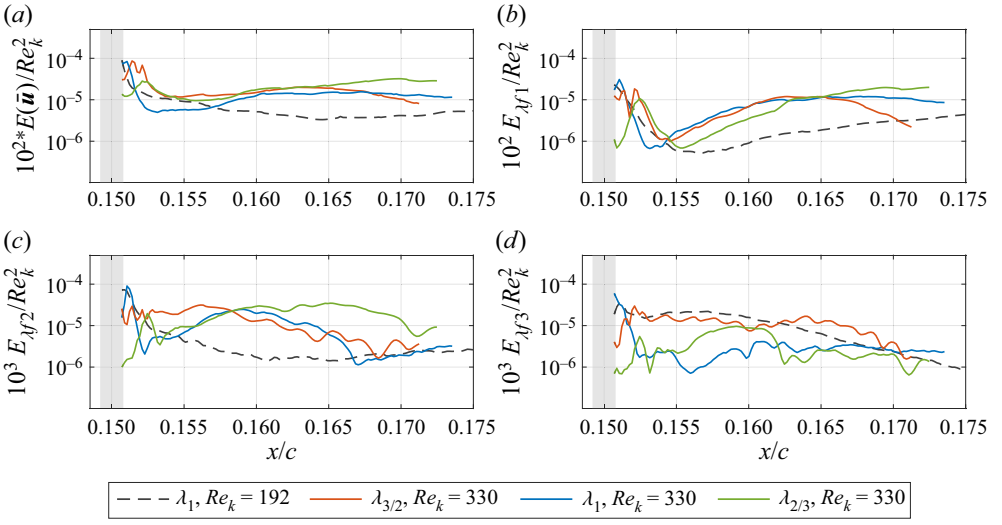

Figure 20. Variation of $E(\bar{\boldsymbol{u}})$ for (*a*) total disturbance fields, (*b*) FFT λ_{f1}, (*c*) λ_{f2} and (*d*) λ_{f3} modes for varying Re_k and λ_{f1}. Energy is scaled by Re_k^2; Element location (grey shaded region).

of the unsteady instabilities dominating the super-critical DRE near wake (e.g. Ergin & White 2006; Loiseau *et al.* 2014; Kuester & White 2016; Zoppini *et al.* 2022*a*).

The scalability of the stationary disturbance energy with Re_k^2 is reported in figure 20 for the considered super-critical configuration, in comparison with the reference critical forcing case (i.e. $\lambda_{f1} = \lambda_1$, $Re_k = 192$). The total disturbance energy shows a larger decay in the element vicinity for the $Re_k = 330$ cases. This can be attributed to the stronger recirculation region developing aft of the DRE, which is in turn related to the increased element height (k_4 for these cases). Nonetheless, the disturbance energy rapidly grows, reaching or overtaking the $Re_k = 192$ values already at $x/c = 0.158$. For all of the presented cases, the evolution of the modal energy associated with the forced wavelength rapidly decays in the element near wake. However, for the super-critical amplitude cases the minimum energy is reached at more upstream chord locations (i.e. at $x/c \simeq 0.155$) with respect to the critical amplitude case. Additionally, the disturbance energy associated with mode λ_{f2} in the $Re_k = 330$ cases shows a substantially different trend when compared with the critical amplitude case, as it undergoes a rapid growth in the element vicinity decaying further downstream. However, the scalability of the energy trends with Re_k^2 is strongly reduced in the super-critical case, especially for the higher harmonics evolution. The lack of trend self-similarity in these super-critical cases is a further indication that the transient growth process is affected by the high unsteadiness and the bypass transition mechanism initiated in the element wake.

Therefore, the receptivity process in critical and super-critical amplitude forcing cases is substantially different. Specifically, in the super-critical case the modal energy evolution shows that the primary stationary mode describes a rapid transient decay, while higher harmonics undergo a transient growth process. Given the increased forcing amplitude, the roughness elements induce a stronger recirculation region and shears that initiate enhanced unsteady disturbances. As such, the combination of the stationary harmonics transient growth, the excessive streak amplitude achieved in the near-wake region, and the enhanced flow unsteadiness are sufficient conditions to initiate the laminar breakdown of the streak structures in the near-wake region. This in turn induces the onset of turbulence, bypassing

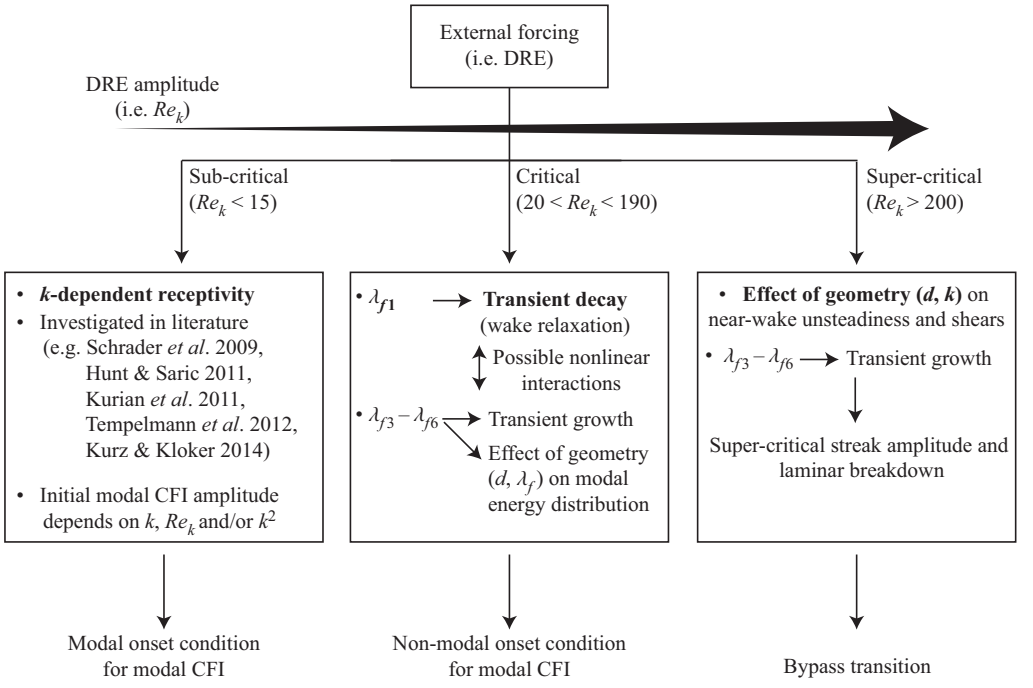

Figure 21. Conceptual sketch of 3-D BL receptivity to external DRE forcing, depending on the external forcing amplitude (i.e. Re_k). Primary stationary disturbance indicated as λ_{f1}, higher harmonics indicated as $\lambda_i = \lambda_{f1}/i$. Main receptivity mechanism for each forcing amplitude range in bold characters.

the development of modal CFI. This behaviour strongly differs from the previously discussed critical amplitude forcing, where the primary stationary mode transient decay is fundamental for the conditioning and onset of the modal instabilities.

5. Conclusion

The near-element flow topology of critical and super-critical DRE in a swept wing BL is detailed, revealing the presence of transient growth in the DRE near wake and characterizing its role in the onset of modal CFI. The 3-D velocity fields in the vicinity of a DRE array are acquired by high-magnification tomographic PTV for a set of Re_k and λ_{f1} configurations. The proposed investigation represents a first effort towards experimentally validating the transient growth model in swept wing BL flows. Furthermore, it results in the production of a conceptual sketch that can be considered as an expansion of the transitional paths model proposed by Morkovin *et al.* (1994), detailing the 3-D BL receptivity to DRE (figure 21).

For the sake of completeness, the conceptual model includes receptivity to sub-critical (not investigated in the present work), critical, and super-critical DRE amplitudes. The investigation of sub-critical configurations is outside the scope of the present work, however, these have been widely characterized in previous studies (e.g. Schrader *et al.* 2009; Hunt & Saric 2011; Tempelmann *et al.* 2012*b*; Kurz & Kloker 2014). These works outlined that sub-critical roughness configurations are well modelled by k-dependent receptivity relationships, which directly correlate the initial CFI amplitude to the roughness height (k/δ^*) or geometrical parameters depending on it (i.e. Re_k). This is summarized by the leftmost branch of the proposed scheme. In the following

discussion, the main findings of the present work on critical and super-critical receptivity are summarized.

The critical near-wake stationary flow topology is characterized by the alternation of low- and high-speed streaks, which are the loci of high-fluctuation regions. As evolving downstream, the amplitude of the streaks reduces, with a single high-speed streak persisting in the flow field and accompanied by the development of a low-speed region on its sides. These structures modulate the BL, resulting in the formation of localized spanwise and wall-normal shears. Spanwise spatial spectral analysis suggests that transient mechanisms dominate the near-wake flow evolution, affecting both the primary stationary mode and its higher harmonics (i.e. smaller wavelengths). Specifically, transient growth affects the chordwise evolution of FFT modes $\lambda_{f3} - \lambda_{f6}$, comparably to what is observed by White *et al.* (2005) in 2-D BLs. Additionally, in this 3-D BL scenario the primary stationary mode (λ_{f1}) evolves following a transient decay process, which can be correlated to the wake relaxation concept proposed by Ergin & White (2006). The dominant mode evolution is well modelled by an initial algebraic decay followed by an exponential growth driven by the inherently unstable nature of the λ_{f1} mode, which essentially evolves into a modal stationary CFI. The identified transient decay and growth processes are robust to Re_k modifications and the corresponding energy evolution is self-similar when scaled by Re_k^2. Nonetheless, they appear to be sensitive to the DRE spacing λ_{f1} and diameter d. Specifically, the combination of λ_{f1} and d conditions the disturbance energy distribution within the FFT spectra. The wavelengths undergoing the most significant transient growth appear to always be included in the $0.7d$–$1.3d$ range. This suggests a correlation between the element geometry, the spatial arrangement of the developing HSV and the observed transient growth in agreement with previous investigations (e.g. Radeztsky *et al.* 1999). Notwithstanding this, all the considered cases show transient decay affecting the λ_{f1} mode.

The identified transient process comprises weak stationary transient disturbances, which allow for the rapid relaxation of the base flow and the development of modal CFI further downstream. Nonetheless, the transient decay of the λ_{f1} mode is fundamental to establishing the onset conditions and downstream evolution of the modal instabilities. More specifically, the CFI onset amplitude estimation (A_0) can be related to the $A_{int,\lambda_{f1}}$ value achieved immediately aft of the near-wake flow region (i.e. the flow region affected by the transient decay mechanism). In this region, the integral amplitude and effective N-factor pertaining to the λ_{f1} CFI mode evolution are well approximated by LST results confirming that the instabilities follow an exponential (thus modal) growth process further downstream. The discussed receptivity scenario for critical DRE amplitudes is summarized by the central branch in figure 21.

To conclude, the near-element flow evolution of a super-critical amplitude DRE is investigated. The near-wake stationary flow topology is dominated by the alternation of high- and low-speed streaks, with the former merging shortly downstream of the element location, substituting the low-speed wake. This results in a stronger and more spread high-fluctuation region, which propagates into a turbulent wedge while evolving downstream. The formation of high- and low-speed streaks cascade on the wake's sides drives the spanwise opening of the turbulent region (Berger & White 2020). The spectral analysis once more highlights the relevant contribution of the stationary transient disturbances to the near-wake development. In the super-critical scenario, steeper decay and growth rates characterize the disturbances' evolution, thus reducing the chordwise extent of the transient process. In this flow scenario, the transient growth process occurs in conjunction with enhanced shears and excessive amplitude of the velocity streaks developing in the near-wake region. Thus, the breakdown of the laminar structures is

initiated shortly downstream of the element, leading to increased flow unsteadiness and the onset of turbulence through bypass transition comparably to what has been previously observed in 2-D BLs (Andersson *et al.* 1999; Reshotko 2001). Accordingly, the role of the transient decay of the λ_{f1} mode becomes secondary in the super-critical scenario, as the onset and evolution of modal CFI is bypassed by the breakdown of the laminar structures. This is in agreement with the reduced scalability offered by Re_k^2 in the super-critical case. The receptivity mechanism identified for super-critical amplitude forcing cases is summarized by the rightmost branch of figure 21, completing the first conceptual map for 3-D BL receptivity to DRE.

Acknowledgements. A dedicated acknowledgement goes to S. Bernardy and E. Langedijk for sharing their technical knowledge during the experimental preparation and to colleagues for their contribution and support.

Funding. The authors are grateful to the European Research Council for financially supporting this research through the GloWing Starting Grant (grant no. 803082).

Declaration of interests. The authors report no conflict of interest.

Author ORCIDs.
G. Zoppini https://orcid.org/0000-0001-7111-9701;
T. Michelis https://orcid.org/0000-0003-4836-6346;
D. Ragni https://orcid.org/0000-0002-8014-5650;
M. Kotsonis https://orcid.org/0000-0003-0263-3648.

References

Acarlar, M.S. & Smith, C.R. 1987 A study of hairpin vortices in a laminar boundary layer. Part 1. Hairpin vortices generated by a hemisphere protuberance. *J. Fluid Mech.* **175**, 1–41.

Andersson, P., Berggren, M. & Henningson, D.S. 1999 Optimal disturbances and bypass transition in boundary layers. *Phys. Fluids* **11** (1), 134–150.

Andersson, P., Brandt, L., Bottaro, A. & Henningson, D.S. 2001 On the breakdown of boundary layer streaks. *J. Fluid Mech.* **428**, 29–60.

Baker, C.J. 1979 The laminar horseshoe vortex. *J. Fluid Mech.* **95** (2), 347–367.

Berger, A.R. & White, E.B. 2020 Experimental Study of the Role of High- and Low-Speed Streaks in Turbulent Wedge Spreading. In *AIAA Scitech 2020 Forum*, p. 832. American Institute of Aeronautics and Astronautics.

Bippes, H. 1999 Basic experiments on transition in three-dimensional boundary layers dominated by crossflow instability. *Prog. Aerosp. Sci.* **35**, 363–412.

Böberg, L. & Brösa, U. 1988 Onset of turbulence in a pipe. *Z. Naturforsch.* **43** (8–9), 697–726.

Breuer, K.S. & Kuraishi, T. 1994 Transient growth in two- and three-dimensional boundary layers. *Phys. Fluids* **6** (6), 1983–1993.

Brynjell-Rahkola, M., Shahriari, N., Schlatter, P., Hanifi, A. & Henningson, D.S. 2017 Stability and sensitivity of a cross-flow-dominated Falkner–Skan–Cooke boundary layer with discrete surface roughness. *J. Fluid Mech.* **826**, 830–850.

Bucci, M.A., Cherubini, S., Loiseau, J.-Ch. & Robinet, J.-Ch. 2021 Influence of freestream turbulence on the flow over a wall roughness. *Phys. Rev. Fluids* **6** (6), 063903.

Casacuberta, J., Groot, K.J., Ye, Q. & Hickel, S. 2019 Transitional flow dynamics behind a micro-ramp. *Flow Turbul. Combust.* **104** (2–3), 533–552.

Cherubini, S., De Tullio, M.D., De Palma, P. & Pascazio, G. 2013 Transient growth in the flow past a three-dimensional smooth roughness element. *J. Fluid Mech.* **724**, 642–670.

Choudhari, M. & Fischer, P. 2005 Roughness-induced transient growth. In *35th AIAA Fluid Dynamics Conference and Exhibit*. American Institute of Aeronautics and Astronautics.

Corbett, P. & Bottaro, A. 2001 Optimal linear growth in swept boundary layers. *J. Fluid Mech.* **435**, 1–23.

Denissen, N.A. & White, E.B. 2013 Secondary instability of roughness-induced transient growth. *Phys. Fluids* **25** (11), 114108.

DOWNS, R.S. & WHITE, E.B. 2013 Free-stream turbulence and the development of cross-flow disturbances. *J. Fluid Mech.* **735**, 347–380.

ERGIN, F.G. & WHITE, E.B. 2006 Unsteady and transitional flows behind roughness elements. *AIAA J.* **44** (11), 2504–2514.

FISCHER, P. & CHOUDHARI, M. 2004 Numerical simulation of roughness-induced transient growth in a laminar boundary layer. In *34th AIAA Fluid Dynamics Conference and Exhibit*. American Institute of Aeronautics and Astronautics.

GREGORY, N.T. & WALKER, W.S. 1956 *The Effect on Transition of Isolated Surface Excrescences in the Boundary Layer*. HM Stationery Office.

HENNINGSON, D.S. 2006 Transient growth with application bypass transition to. In *IUTAM Symposium on Laminar-Turbulent Transition* (ed. R. Govindarajan), pp. 15–24. Springer.

HERBERT, T. 1993 Parabolized stability equations. In *AGARD: Special Course on Progress in Transition Modelling, AGARD-R-d793*, p. 4. NATO.

HUNT, J.C.R., WRAY, A.A. & MOIN, P. 1988 Eddies streams and convergence zones in turbulent flows. In *Studying Turbulence Using Numerical Simulation Databases-II*, p. 193. Center for Turbulence Research.

HUNT, L. & SARIC, W. 2011 Boundary-layer receptivity of three-dimensional roughness arrays on a swept-wing. In *41st AIAA Fluid Dynamics Conference and Exhibit*, p. 3881.

JANKE, T. & MICHAELIS, D. 2021 Uncertainty quantification for PTV/LPT data and adaptive track filtering. In *14th International Symposium on Particle Image Velocimetry*, vol. 1 (1).

KENDALL, J.M. 1981 Laminar boundary layer velocity distortion by surface roughness: effect upon stability. *AIAA Paper* **195**, 1981.

KLEBANOFF, P.S., CLEVELAND, W.G. & TIDSTROM, K.D. 1992 On the evolution of a turbulent boundary layer induced by a three-dimensional roughness element. *J. Fluid Mech.* **237**, 101–187.

KUESTER, M.S. & WHITE, E.B. 2016 Structure of turbulent wedges created by isolated surface roughness. *Exp. Fluids* **57**, 1–13.

KUESTER, M.S. & WHITE, E.B. 2015 Roughness receptivity and shielding in a flat plate boundary layer. *J. Fluid Mech.* **777**, 430–460.

KURZ, H.B.E. & KLOKER, M.J. 2014 Receptivity of a swept-wing boundary layer to micron-sized discrete roughness elements. *J. Fluid Mech.* **755**, 62–82.

KURZ, H.B.E. & KLOKER, M.J. 2016 Mechanisms of flow tripping by discrete roughness elements in a swept-wing boundary layer. *J. Fluid Mech.* **796**, 158–194.

LANDAHL, M.T. 1980 A note on an algebraic instability of inviscid parallel shear flows. *J. Fluid Mech.* **98** (2), 243–251.

LEVIN, O. & HENNINGSON, D.S. 2003 Exponential vs algebraic growth and transition prediction in boundary layer flow. *Flow Turbul. Combust.* **70** (1–4), 183–210.

LOISEAU, J.C., ROBINET, J.C., CHERUBINI, S. & LERICHE, E. 2014 Investigation of the roughness-induced transition: global stability analyses and direct numerical simulations. *J. Fluid Mech.* **760**, 175–211.

LUCAS, J.M. 2014 Spatial optimal perturbations for transient growth analysis in three-dimensional boundary layers. PhD thesis, Universite de Toulouse.

MACK, L.M. 1984 Boundary-layer linear stability theory. *Tech. Rep.* ADP004046. California Institute of Technology Pasadena Jet Propulsion Laboratory.

MALIK, N.A. & DRACOS, T. 1993 Lagrangian PTV in 3D flows. *Appl. Sci. Res.* **51** (1), 161–166.

MORKOVIN, M.V. 1969 On the many faces of transition. In *Viscous Drag Reduction* (ed. C. Sinclair Wells), pp. 1–31. Springer.

MORKOVIN, M.V., RESHOTKO, E. & HERBERT, T. 1994 Transition in open flow systems-a reassessment. *Bull. Am. Phys. Soc.* **39**, 1882.

MUNARO, F. 2017 Mechanisms of boundary layer transition due to isolated roughness on swept wings: an experimental study. Master thesis, Technische Universiteit Delft.

RADEZTSKY, R.H., REIBERT, M.S. & SARIC, W.S. 1999 Effect of isolated micron-sized roughness on transition in swept-wing flows. *AIAA J.* **37** (11), 1370–1377.

REIBERT, M., SARIC, W.S., CARRILLO, R. JR. & CHAPMAN, K. 1996 Experiments in nonlinear saturation of stationary crossflow vortices in a swept-wing boundary layer. In *34th Aerospace Sciences Meeting and Exhibit*. American Institute of Aeronautics and Astronautics.

RESHOTKO, E. 2001 Transient growth: a factor in bypass transition. *Phys. Fluids* **13** (5), 1067–1075.

RIZZETTA, D.P., VISBAL, M.R., REED, H.L. & SARIC, W.S. 2010 Direct numerical simulation of discrete roughness on a swept-wing leading edge. *AIAA J.* **48** (11), 2660–2673.

SARIC, W.S., CARRILLO, R. & REIBERT, M. 1998 Leading-edge roughness as a transition control mechanism. In *36th AIAA Aerospace Sciences Meeting and Exhibit*, p. 781.

SARIC, W.S., REED, H.L. & WHITE, E.B. 2003 Stability and transition of three dimensional boundary layers. *Annu. Rev. Fluid Mech.* **35** (1), 413–440.

SARIC, W.S., WEST, D.E., TUFTS, M.W. & REED, H.L. 2019 Experiments on discrete roughness element technology for swept-wing laminar flow control. *AIAA J.* **57** (2), 641–654.

SCHANZ, D., GESEMANN, S. & SCHRÖDER, A. 2016 Shake-the-box: Lagrangian particle tracking at high particle image densities. *Exp. Fluids* **57** (5), 1–27.

SCHANZ, D., GESEMANN, S., SCHRÖDER, A., WIENEKE, B. & NOVARA, M. 2012 Non-uniform optical transfer functions in particle imaging: calibration and application to tomographic reconstruction. *Meas. Sci. Technol.* **24** (2), 024009.

SCHMID, P.J. & HENNINGSON, D.S. 2001 *Applied Mathematical Sciences*. Springer.

SCHRADER, L.U., BRANDT, L. & HENNINGSON, D.S. 2009 Receptivity mechanisms in three-dimensional boundary-layer flows. *J. Fluid Mech.* **618**, 209–241.

SERPIERI, J. 2018 Cross-flow instability. PhD thesis, Technische Universiteit Delft.

SERPIERI, J. & KOTSONIS, M. 2015 Design of a swept wing wind tunnel model for study of cross-flow instability. In *33rd AIAA Applied Aerodynamics Conference*. American Institute of Aeronautics and Astronautics.

SERPIERI, J. & KOTSONIS, M. 2016 Three-dimensional organisation of primary and secondary crossflow instability. *J. Fluid Mech.* **799**, 200–245.

TANI, I. 1969 Boundary-layer transition. *Annu. Rev. Fluid Mech.* **1** (1), 169–196.

TEMPELMANN, D., HANIFI, A. & HENNINGSON, D.S. 2012*a* Spatial optimal growth in three-dimensional compressible boundary layers. *J. Fluid Mech.* **704**, 251–279.

TEMPELMANN, D., SCHRADER, L.U., HANIFI, A., BRANDT, L. & HENNINGSON, D.S. 2012*b* Swept wing boundary-layer receptivity to localized surface roughness. *J. Fluid Mech.* **711**, 516–544.

VON DOENHOFF, A.E. & BRASLOW, A.L. 1961 The effect of surface roughness on laminar flow. In *Boundary Layer and Flow Control*, pp. 657–681. Elsevier.

WASSERMANN, P. & KLOKER, M. 2002 Mechanisms and passive control of crossflow-vortex-induced transition in a three-dimensional boundary layer. *J. Fluid Mech.* **456**, 49–84.

WHITE, E.B. & ERGIN, F.G. 2003 Receptivity and transient growth of roughness induced disturbances. In *33rd AIAA Fluids Dynamics Conference and Exhibit*, p. 4243.

WHITE, E.B., RICE, J.M. & ERGIN, F.G. 2005 Receptivity of stationary transient disturbances to surface roughness. *Phys. Fluids* **17** (6), 064109.

WIENEKE, B. 2008 Volume self-calibration for 3D particle image velocimetry. *Exp. Fluids* **45** (4), 549–556.

WIENEKE, B. 2012 Iterative reconstruction of volumetric particle distribution. *Meas. Sci. Technol.* **24** (2), 024008.

YE, Q., SCHRIJER, F.F.J. & SCARANO, F. 2016 Geometry effect of isolated roughness on boundary layer transition investigated by tomographic PIV. *Intl J. Heat Fluid Flow* **61**, 31–44.

ZOPPINI, G., RAGNI, D. & KOTSONIS, M. 2022*a* Transition due to isolated roughness in a swept wing boundary layer. *Phys. Fluids* **34** (8), 084113.

ZOPPINI, G., WESTERBEEK, S., RAGNI, D. & KOTSONIS, M. 2022*b* Receptivity of crossflow instability to discrete roughness amplitude and location. *J. Fluid Mech.* **939**, A33.